



RESEARCH ARTICLE

10.1029/2023GC010860

Key Points:

- Two-phase flow models of crustal magmatic systems identify two modes: batholith emplacement versus convective recycling of evolved rock
- High melt mobility, multiple heating pulses, and low density of solidified evolved rock favor batholith emplacement
- The Altiplano-Puna low-velocity zone (LVZ) is in the batholith emplacement mode and the Tibetan LVZ is in the convective recycling mode

Supporting Information:

Supporting Information may be found in the online version of this article.

Correspondence to:

H. Schmeling,
Schmeling@geophysik.uni-frankfurt.de

Citation:

Schmeling, H., Marquart, G., Weinberg, R., & Kumaravel, P. (2023). Dynamic two-phase flow modeling of melt segregation in continental crust: Batholith emplacement versus crustal convection, with implications for magmatism in thickened plateaus. *Geochemistry, Geophysics, Geosystems*, 24, e2023GC010860. <https://doi.org/10.1029/2023GC010860>

Received 10 JAN 2023

Accepted 15 APR 2023

Author Contributions:

Conceptualization: Harro Schmeling, Gabriele Marquart, Roberto Weinberg
Data curation: Harro Schmeling, Gabriele Marquart, Roberto Weinberg
Formal analysis: Harro Schmeling, Gabriele Marquart, Roberto Weinberg
Funding acquisition: Harro Schmeling

© 2023. The Authors. *Geochemistry, Geophysics, Geosystems* published by Wiley Periodicals LLC on behalf of American Geophysical Union. This is an open access article under the terms of the [Creative Commons Attribution-NonCommercial-NoDerivs License](https://creativecommons.org/licenses/by-nc-nd/4.0/), which permits use and distribution in any medium, provided the original work is properly cited, the use is non-commercial and no modifications or adaptations are made.

Dynamic Two-Phase Flow Modeling of Melt Segregation in Continental Crust: Batholith Emplacement Versus Crustal Convection, With Implications for Magmatism in Thickened Plateaus

Harro Schmeling¹ , Gabriele Marquart⁵, Roberto Weinberg¹ , and Pirunthavan Kumaravel^{2,3}

¹School of Earth, Atmosphere and Environment, Monash University, Clayton, VIC, Australia, ²Now at Institute of Geosciences, Goethe University Frankfurt, Frankfurt, Germany, ³Now at Institute of Georesources Management, RWTH Aachen University, Aachen, Germany, ⁴Retired Institute of Geosciences, Goethe University Frankfurt, Frankfurt, Germany, ⁵Retired Institute for Applied Geophysics and Geothermal Energy, E.ON Energy Research Center, RWTH Aachen University, Aachen, Germany

Abstract Magmatic processes in the continental crust such as crustal convection, melt ascent, magma emplacement, and batholith formation are not well understood. We solve the conservation equations for mass, momentum, and energy for two-phase flow of melt and solid in 2D, for a thick continental crust heated from below by one or several heat pulses. A simplified binary melting model is incorporated. We systematically vary (a) the retention number, characterizing melt mobility, (b) the intensity of heat pulses applied at the bottom, and (c) the density of the solidified evolved rock. Two characteristic modes are identified: (a) in the “batholith emplacement mode,” segregation is sufficiently strong allowing melts to separate from the convective flow. This melt freezes to form buoyant SiO₂-rich layers. (b) In the “convective recycling mode,” melts are formed in the lower crust, rise together with the hot rock with little segregation, freeze at shallow depth but are partly recycled back to the lower crust where they remelt. Phase-change-driven convection dominates. Mode (a) is favored by high heat input, multiple heat pulses, high melt mobility, and low density of the evolved rock. Mode (b) is favored by less intense heating, less melt mobility, and denser evolved rocks. A scaling law is derived based on the thermal, melt, and compositional Rayleigh numbers and the retention number. The Altiplano-Puna low-velocity zone (LVZ) could represent the batholith emplacement mode with buoyant and voluminous magmas causing intense volcanism. The Tibetan LVZ is not associated with intense volcanism and might represent the convective recycling mode.

1. Introduction

Granite batholiths and smaller intrusions of a wide range of geological ages are common in the continental crust worldwide. There is a long-lasting debate about the origin of granites (e.g., Read, 1948), which has intensified in recent years (Jagoutz & Klein, 2018; Moyen et al., 2021). The two generic endmembers are granites being a result of fractionation from mantle-derived magmas or granites being the product of partial melting and melt segregation of continental crustal rocks. In this paper, we address the latter process and focus on the impact of pulses of heat at the crust—mantle boundary on the formation of evolved magmas. In particular, we address the mechanism responsible for possible emplacement of batholiths or convective recycling of partially molten rocks.

Granite batholiths have been proposed to be genetically related to high-grade metamorphic rocks (e.g., Othman et al., 1984; Wells, 1981). The formation of silicic melt in the lower crust and ascent to shallower depth is assumed to be a primary process of crustal differentiation (e.g., Wells, 1980). Granitoid emplacement has been recorded in ancient and active magmatic systems in various regions of the Earth, such as in the Andes (e.g., Ward et al., 2014), Tibet (e.g., Nelson et al., 1996; Unsworth et al., 2005) or in Tuscany, Italy (e.g., Puxeddu, 1984) and provide key observations for understanding the dynamics of crustal magmatic systems and formation of batholiths.

Geophysical and geological observations in such active magmatic systems have been reviewed by Cashman et al. (2017) and include enhanced surface heat flow, decreased electrical resistivity, and, if enough eruptible melt is generated, ignimbrite surface eruptions. For the Central Andes, Springer and Förster (1998) and Springer (1999) reported heat flux values between 50 and 180 mW/m². Low electrical resistivities of 3 Ωm near 20 km depth

Investigation: Harro Schmeling, Gabriele Marquart, Roberto Weinberg, Pirunthavan Kumaravel

Methodology: Harro Schmeling, Gabriele Marquart, Pirunthavan Kumaravel

Software: Harro Schmeling

Validation: Harro Schmeling, Pirunthavan Kumaravel

Visualization: Harro Schmeling, Gabriele Marquart

Writing – original draft: Harro Schmeling, Gabriele Marquart, Roberto Weinberg

Writing – review & editing: Roberto Weinberg

in the Altiplano (Comeau et al., 2015) have been explained by 20%–100% melt depending on the water content (Schmeling et al., 2019). From surface wave and receiver function data a large low-shear-velocity body between 4 and 25 km depth has been found beneath the Altiplano-Puna Volcanic Complex (APVC) and interpreted to have up to 25% of partial melt (Ward et al., 2014). Based on a joint interpretation combined with thermomechanical modeling, Spang et al. (2021) estimated melt fractions between 15% and 22%. Large volumes of ignimbrites have been erupted during the last 11 Ma (Perkins et al., 2016). The thermal structure of the Altiplano-Puna Magmatic Body has been reviewed, including geophysical and petrological data, by Gottsmann et al. (2017). They inferred a reference geotherm reaching 750°C at 25 km depth and an elevated geotherm within the magmatically active plumbing system, which is hotter than the reference geotherm by 200–350 K.

From such observations, a picture of continental magmatic systems has emerged consisting of vertical sequences of mush bodies with interstitial melts increasing upwards in SiO₂ content. These mush bodies are sometimes covered by melt-rich caps, connected by magma conduits (Bachmann & Huber, 2016; Cashman et al., 2017; de Silva et al., 2015). While the uppermost mush and associated melt cap bodies have been constrained by geophysical methods (seismic, magnetotelluric methods) as mentioned above, deeper mush bodies are difficult to identify.

The existence of such deep sequences including stacked bodies of mush and magma with variable SiO₂ content has been proposed by for example, Cashman et al. (2017). Such stacking in a dynamic system is only possible under certain conditions and requires a special thermal, density, and rheological structure in the crust to be gravitationally stable at least over some 10⁵ years. So far most of the models investigating the thermal structure of magmatic systems (e.g., Annen et al., 2006, 2015; Blundy & Annen, 2016; Sparks et al., 2019) have been based on the intrusion of hot magma sills, experimenting with the rate of intrusion and different initial crustal conditions, like crustal thickness or thermal structure. They have considered neither the dynamics nor the stability of such stacked layers of various densities and viscosities, nor the large-scale crustal ductile deformation and flow. For a single hot mush layer, time scales of a Rayleigh-Taylor instability have been estimated to match the ranges typical for episodic volcanism (Seporian et al., 2018). van Zalinge et al. (2022) extended this approach and combined such Rayleigh-Taylor time scales with parameterized magma conduit models to explain observed repose times of ignimbritic episodic eruptions of order 1 Ma in the Oxaya formation (Central Andes). With such timescales in mind, we designed our model approach: We investigate in a dynamically consistent numerical model with an Andean-like crustal structure, the possible development of granitic batholiths triggered by either a single long-lasting or multiple short-duration heating events at the bottom of the model (crust-mantle boundary). We will test possible mechanisms of generating mush bodies in dynamic systems activated by single or multiple heat pulses at Moho depth, leading to partial melting and buoyancy that leads to crustal convection and rising melt capable of segregating to form magmatic bodies or batholiths.

A prerequisite for active magmatic systems in continental crust and the generation of silicic melt is a high heat input or a volatile influx from the mantle. For a thickened crust, such as in collision belts, radioactive heat at depth might be enough to allow partial melting and weak diapirism (Arnold et al., 2001). Another possible heat source to initiate partial melting in the lower continental crust is a sudden heat input from the mantle by underplating or sill intrusion of mantle-derived basaltic material (Annen et al., 2006; Riel et al., 2016; Thybo & Artemieva, 2013). The nature and temporal behavior of such heating events control the magmatic evolution of the overlying crust. In a model setup representing a thick continental crust, heating events associated with underplating may be realized by temporal variations of thermal bottom boundary conditions. In principle, two end-members of heating modes can be distinguished: elevated bottom temperature or elevated bottom heat flux over given durations. If heating is associated with underplating of voluminous basaltic melts, the overlying crust experiences elevated temperatures of the order of the solidus temperature of basaltic melts. If underplating occurs sporadically and is characterized by episodes of basalt emplacement followed by complete crystallization, the bottom crustal temperature may be time-dependent, and the mode of heat source may be better described by an enhanced heat flux condition at the bottom of the crust of a given duration. The latter heating mode is used here. Advective heat addition to the crust by mafic melt influx from the mantle is not modeled explicitly. In subduction related continental magmatism volatile influx may originate from dewatering of subducted oceanic crust (e.g., Wyllie, 1984) or volatile release due to solidification of underplating of mafic melts (Annen et al., 2006). While this mechanism is important for lowering the solidus temperature of lower continental crust (e.g., R. F. Weinberg & Hasalová, 2015), we neglect it and subsume volatile influx under one effective heat influx rate and choosing appropriate simplified melting curves as in Schmeling et al. (2019).

Zircon U-Pb ages are important time markers that constrain the time-dependence of crustal heating events and magmatism in subduction-related orogens. They show that magmatism is not a steady process resulting from constant heat input from the mantle, but it is generally characterized by a hierarchy of multiscale episodicities. For example, the Tuolumne Intrusive Suite (Sierra Nevada) shows a flare-up of magmatic activity lasting about 10 Ma modulated by about three maxima of about 1–3 Ma duration (de Silva et al., 2015). Single plutons, such as the 8 km wide Torres del Paine intrusive complex (Patagonia), have formed during only 0.2 Ma (Leuthold et al., 2012). The magmatic system of the Oxaya Formation (Central Andes) has lasted at least 7.7 Ma starting with a period of 4.6 Ma of pluton growth, followed by episodic ignimbrite eruptions on a time scale of 1 Ma (van Zalinge et al., 2022). During the long-term subduction history of the Andes, the APVC ignimbrite flare-up represents a waning and then waxing pulse of about 10 Ma duration and is subdivided into four magmatic pulses of about 2 Ma duration, while the individual ignimbrite zircon spectra define shorter pulses of <1 Ma (Kern et al., 2016). Lifetimes of APVC magmas of about 0.4 Ma have been determined by dating the eruption of individual ignimbrites (Kern et al., 2016). Such a spectrum of episodicities represents surface or middle-to-upper crustal magmatic pulses and may be the result of crustal modulation of smoother mantle pulses (de Silva et al., 2015). This is the motivation for our models testing both single, long-lasting and multiple, shorter mantle heat pulses.

As temperatures become elevated, silicic melts on the order of a few volume percent or more are generated in the lower crust and ascends driven by buoyancy. Consequently, silicic material accumulates at shallower depths, leaving behind more residual material in the lower crust. The style of melt ascent at depth will mainly depend on melt fraction, melt viscosity, permeability of the melt network and solid matrix rheology. Possible scenarios include convective rising of partially molten mushes driven by thermal and melt buoyancy with or without caps of accumulated melt, or distributed melt segregation with melt channeling and veining. If melt caps are present, melt carrying heat might infiltrate further into the roof of the melt caps and rise further by a mechanism involving decompaction and sinking of solid roof material with respect to the rising melt (stopping or micro-stopping, Schmeling et al., 2019; Weinberg et al., 2021). Schmeling et al. (2019) called this mechanism “Compaction/decompaction Assisted Two-phase flow Melt Ascent” (CATMA). The extent to which melt accumulates to form stable evolved, granitoid bodies or layers also depends on the density contrast between the solidified felsic material and the original crust. This will be one key parameter for the models shown below.

Once melt caps or mush bodies with high melt fraction reach the transition to the brittle crust, ductile fracturing, compaction instabilities, dyke formation, and rapid dyke ascent might occur, possibly supported by an extensional tectonic setting of the crust (Rivalta et al., 2015; Rubín, 1993; Rummel et al., 2020). In this study, we focus on how the deeper processes of mush formation, melt accumulation, and batholith formation depend on the heating mode (single or multiple heating event), heating intensity, melt mobility, and density of the solidified enriched material. We neglect dyking and the changes it may bring to the system.

Ascending melts may not always accumulate and be directly extracted, but may instead undergo several cycles of solidification, reworking and remelting. For Himalayan and Karakoram leucogranites, Weinberg (2016) found that typically zircon date ranges in individual samples or multiple samples vary by as much as 10 Ma. They summarized the different hypotheses in the literature used to explain these age ranges: “(a) *multiple events of partial resorption and regrowth of monazite and zircon during anatexis due to evolving metamorphic reactions* (Rubatto et al., 2013), (b) *physical remobilization of early formed grains in migmatites and leucogranites by new magma pulses, in an environment of fluctuating melt fraction* (Lederer et al., 2013; Viskupic et al., 2005), (c) *mixing of ages due to hybridization and magma mixing* (Hasalová et al., 2013), and (d) *prolonged fractionation and cooling of granites* (Horton & Leech, 2013). Combined, the data suggest that the volumes of melt present in the crust at any time were relatively small, being accumulated, reworked and remobilized several times over the duration of anatexis.” This opens the question about the physical conditions and temporal heating modes responsible for such magma accumulations forming evolved granites, possibly being recycled and reworked by crustal convection.

Elaborating this further, rising magmatic bodies may not always be emplaced as mushy zones or batholiths within the crust, instead they may return to the deeper crust in the downwelling limbs of crustal convection where they may undergo remelting. We will call this process recycling. Crustal convection has been described by for example, Vanderhaeghe et al. (2018), Babeyko et al. (2002), and Weinberg (1997). In their dynamic models Louis-Napoléon et al. (2022) approximated partially molten regions by meso-scale inclusions and identified different flow regimes depending essentially on the choice of viscosities. In the suspension regime the

inclusions remained entrained in the convection, while in the layering regime they accumulated beneath a crustal lid. Petrological signatures for recycling could include mixing of primitive magmas with a granitic melt, assimilation of country rock, and age differences between ages of the protolith of a granitic pluton and remelting events (e.g., Jagoutz & Klein, 2018). Trace element variations within individual magma reservoirs of the APVC suggest differences in melt fractions and melt compositions (Kern et al., 2016) which could be a sign of multiple remixing during convection. However, no emphasis has been placed on which physical conditions would control whether rising silicic magma would be emplaced as batholiths or whether felsic magmatic rocks would be recycled back into the lower crust/source zone through convection. One aim of this study is to identify parameter ranges which lead to magma ascent followed by batholith emplacement and those that lead to ongoing convective overturns and recycling. Here the term convection is used in a broad sense, either driven by thermal, phase change (melting-freezing), and compositional (enriched-depleted rock) density variations.

In this paper we will use the following notation: melts or magmatic rocks that have been differentiated from a fertile original lower crust may be called synonymously evolved, silicic, felsic, fractionated, or enriched (in SiO_2), while the residual material may be called residual, restitic or depleted (in SiO_2). Because our two-phase-flow formulation is originally based on mantle melting, we prefer keeping the mantle dynamics notation and mostly use “enriched” and “depleted,” referring to the SiO_2 -content, describing the two compositions mentioned above. In our formulation, fully enriched and fully depleted rocks contain finite amounts of SiO_2 , detailed in Section 2.2.

In Section 2, the numerical model approach is described. In Section 3.1, we present a typical model with a single and with pulsed heating events and investigate models representing the two modes: “convective recycling” versus “batholith emplacement.” Sections 3.2–3.4 explore the effects of melt mobility (i.e., melt viscosity), intensity of heat input and density of enriched rock with focus on convective recycling versus batholith emplacement. These two modes are analyzed in detail in Appendix D. In Section 3.5, the full parameter space is explored to identify the regimes in which either of these two modes dominates. In Section 3.6 an analytical scaling law for the boundary between these two modes is derived. Section 4 discusses the limitations, the role of pulse frequency and duration, and applies the models to observations of natural magmatic systems and concludes the study.

2. Model Approach

We investigate melting and melt segregation in the continental crust by numerical modeling of two-phase flow including de/compaction of the solid matrix. Starting with McKenzie (1984) such flows have been formulated for small melt fractions, but recently they have been extended to moderate or even high melt fractions (Keller & Suckale, 2019; Schmeling et al., 2019; Wong & Keller, 2023). We build on the formulation of Schmeling et al. (2019) and assume a single heat pulse or a sequence of heat pulses at the base of an initially unmolten fertile continental crust. We assume a thick continental crust, typical of convergence belts as in the Andes or Tibet. We study the generation, ascent and freezing of melt, and the development of batholiths in the middle and upper crust. As discussed in the introduction, we prefer a heat flow boundary condition over a sudden temperature increase, because this seems to us more natural and allows a better control of the energy input into the model. Indeed, switching on and off the anomalous temperature would also switch the direction of heat flow at the base of the crust from upward to an unreasonable downward heat flow at the Moho.

Our modeling approach is based on the thermo-mechanical two-component two-phase flow formulation of a melt/solid system described in Schmeling et al. (2019). The two phases are solid and melt, with φ as the volumetric melt fraction or melt porosity. Low viscosity melt is allowed to move with respect to the highly viscous flowing solid, and the compositions of melt and solid are advected independently and may vary between depleted (SiO_2 -poor) and enriched (SiO_2 -rich) according to a melting law. Here we provide only the basics of the formulation and those assumptions, which differ from Schmeling et al. (2019).

2.1. Mathematical Formulation

The formulation includes the conservation equations of mass, momentum, and composition for the melt and solid, and of energy (as in Schmeling et al. (2019)) based originally on McKenzie (1984) and includes viscous compaction and decompaction of the solid matrix. They are given in Appendix A and B. The low melt viscosity approximation is used, implying that viscous stresses within the melt phase are neglected with respect to the viscous stresses in the solid. Melt movement with respect to the solid is controlled by Darcy flow with a Kozeny-Carman

type permeability—porosity relation $k = \frac{d^2}{C} \phi^{n_\phi}$ with a power of $n_\phi = 3$, where C is a geometric factor of the order of 100 depending on the actual pore geometry, and d is the mean distance of the pores (often equal to the grain size). Melt viscosity (\ll solid viscosity) is assumed constant and the formulation includes the compaction pressure (second term in Equation A6 (Appendix A), see also Schmeling et al. (2019) and Katz et al. (2007)). The densities of the solid ρ_s and melt ρ_f depend on temperature and composition using two linear equations of state

$$\rho_s = \rho_0(1 - \alpha T - \beta_{d|e} f) \quad (1)$$

$$\rho_f = \rho_0(1 - \alpha T - \beta_f) \quad (2)$$

where ρ_0 is the reference solid density, α is the thermal expansivity, T is the temperature, f is the depletion (if $f > 0$) or enrichment (if $f < 0$) in SiO_2 with respect to the initial composition (see Section 2.2), $\beta_{d|e} = \frac{\rho_0 - \rho_{dp}}{\rho_0}$ or $\beta_{d|e} = -\frac{\rho_0 - \rho_{enr}}{\rho_0}$ depending on whether $f > 0$ or $f < 0$, respectively, and $\beta_f = \frac{\rho_0 - \rho_{0f}}{\rho_0}$ is the scaled reference solid—melt density difference. See also Table 1 for the definitions of symbols. The mixture density is defined as

$$\rho = \varphi \rho_f + (1 - \varphi) \rho_s \quad (3)$$

where φ is the volumetric melt fraction. A kind of Boussinesq approximation is applied, assuming the incompressibility of the solid and fluid phases and constant density in all terms except the buoyancy terms in the momentum equation of the mixture and the Darcy equation (as in Schmeling et al. (2019)). This implies that the mass divergence of the mixture is always zero, even during melting and solidification, but the divergence of the solid matrix is non-zero due to compaction/decompaction. The Boussinesq approximation is applicable as long as density variations are below about 10%. The viscosity of the porous matrix depends on temperature, depth, and stress using a visco-plastic power-law rheology (Equations A8–A10 (Appendix A)), and porosity following Schmeling et al. (2012) (Equation A11 (Appendix A)). See also Schmeling et al. (2019)). The energy conservation equation neglects adiabatic and viscous heating but includes depth-dependent radiogenic heating and latent heat due to melting and solidification (Equation A5 (Appendix A)). Local thermal equilibrium between melt and solid is assumed, and the advective velocity assumes a melt porosity (i.e., a melt fraction) weighted mean of the solid and melt velocities (Equation A7 (Appendix A)). All equations are non-dimensionalized which results in four Rayleigh numbers for bottom heat flux, melt, enrichment, and depletion, respectively, and a retention number

$$\text{Ra}_q = \frac{\rho_0 \alpha g q h^4}{\lambda \kappa \eta_0}, \text{Ra}_f = \frac{(\rho_0 - \rho_{0f}) g h^3}{\kappa \eta_0}, \text{Ra}_{enr} = \frac{(\rho_0 - \rho_{enr}) g h^3}{\kappa \eta_0}, \text{Ra}_{dp} = \frac{(\rho_{dp} - \rho_0) g h^3}{\kappa \eta_0}, \text{Rt} = \frac{C \eta_f h^2}{\eta_0 d^2} \quad (4)$$

where $\rho_0, \rho_{0f}, \rho_{enr}, \rho_{dp}$ are the densities of the undepleted or reference rock, of the melt, of the fully enriched rock, and of the fully depleted rock, respectively, α is the thermal expansivity, g is the gravitational acceleration, q is the bottom heat flux, h is the model height, λ is the thermal conductivity, κ is the thermal diffusivity, η_0, η_f are the reference and melt viscosities, respectively, C is a geometric factor of the order of 100 depending on the actual pore geometry, and d is the mean distance of the pores (often equal to the grain size). The inverse of the retention number is proportional to d^2/η_f which describes the mobility of the melt with respect to the solid matrix. A high retention number corresponds to immobile melts, that is, melts which are retained in the matrix. For typical wet granitic melt viscosities (10^4 – 10^7 Pa s) and d in the range of 1 mm–10 cm the retention number ranges between 1 and 100 (see the discussion in Schmeling et al., 2019). In this study we investigate the effects of the retention number Rt , the bottom heat flux in terms of Ra_q , and the enriched density in terms of Ra_{enr} on the dynamics of crustal melt transport.

2.2. Chemical Composition, Melting Law, and Rock Physical Parameters

As in Schmeling et al. (2019), we assume an initially uniform, thickened fertile continental crust typical of orogenic belts. The composition of meta-greywacke is assumed containing quartz, plagioclase, and biotite, regarded as a protolith of granitic melts. With ongoing melting, melt segregation, and solidification, the rock types evolve both into more depleted, SiO_2 -poor granulite facies residual rocks, and more enriched, SiO_2 -rich granitic rocks after the melt solidifies.

We use an approximative melting law which is based on the physics of a binary solid solution phase diagram with the components A representing “evolved, differentiated, silicic, felsic rock or melt” and B representing “residual, restitic rock.” As noted in Section 1, these terms are used synonymously, and we will use the term

Table 1
Symbols, Their Definition, Numerical Values, and Physical Units Used in This Study

Symbol	Definition	Value	Units
A_{duc}	Pre-factor in solid ductile viscosity	0.001	$\text{MPa}^n \text{s}^{-1}$
A	Byerlee law constant	10^4	Pa m^{-1}
B	Byerlee law constant	20	MPa
c_p	Specific heat capacity, equal for all rock types	1,000	$\text{J kg}^{-1} \text{K}^{-1}$
c, c_0, c_f, c_s	Mass fractions of component B (see Figure 1): mixture, initial, fluid phase, solid phase		–
C	Geometric factor relating permeability to grain size	100	–
d	Mean distance between pores (grain size)	See Rt	m
e	Enrichment field, $e = -f$ if $f < 0$		–
E	Activation energy	$167 \cdot 10^3$	J mol^{-1}
e_b	Batholith emplacement parameter	0 to 1	–
\dot{e}_{II}	Second invariant of solid strain rate tensor	Variable	s^{-1}
f	Depletion (if > 0) or enrichment (if < 0) field		–
\bar{g}	Gravity acceleration	10	m s^{-2}
h	Scaling length (here height of the model)	50,000	m
H	Radioactive heat production rate in the crust, $H(z)$	Variable	W kg^{-1}
k	Permeability depending on porosity (i.e. melt fraction)	Variable	m^2
L	Latent heat	300	kJ kg^{-1}
n_ϕ	Exponent of the porosity-permeability relation	3	–
n	Stress exponent	2	–
P	Pressure	Variable	Pa
P_{lith}	Lithostatic pressure = $\rho_0 g(h - z)$	Variable	Pa
q	Mantle or bottom heat flux	Variable	W m^{-2}
q_0	Initial or background bottom heat flux	0.0295	W m^{-2}
q_{pulse}	Elevated bottom heat flux during a heat pulse	Variable	W m^{-2}
R	Gas constant	8.31	$\text{J mol}^{-1} \text{K}^{-1}$
$\text{Ra}_q, \text{Ra}_f, \text{Ra}_{\text{enr}}, \text{Ra}_{\text{dp}}$	Rayleigh number for heat (q), melt phase (f), enriched rock (enr), depleted rock (dp)		–
Rt	Retention number	1 to 100	–
t	Time		s
T, T_{abs}	Temperature, absolute temperature	Variable	$^\circ\text{C}$
\bar{v}	Mean velocity of solid and fluid	Variable	m s^{-1}
\bar{v}_f	Fluid (i.e. melt) velocity	Variable	m s^{-1}
\bar{v}_s	Solid velocity	Variable	m s^{-1}
\bar{v}_{sgr}	Segregation velocity, $\bar{v}_{\text{sgr}} = \bar{v}_f - \bar{v}_s$	Variable	m s^{-1}
V	Activation volume	10^{-5}	$\text{m}^3 \text{mol}^{-1}$
x	Horizontal coordinate		m
z	Vertical coordinate (positive upward)		m
\bar{z}	Depth		m
α	Thermal expansivity (equal for all rock types)	$2.4 \cdot 10^{-5}$	K^{-1}
$\beta_f, \beta_d, \beta_e$	Density contrast factors for fluid phase (f), depleted rock (d), enriched rock (e)	0.1481, -0.1481 , -0.037	–
Γ	Rate of melt generation or solidification	Variable	$\text{kg m}^{-3} \text{s}^{-1}$
η_0	Reference (scaling) viscosity	10^{20}	Pa s
η_b	Effective bulk viscosity of the porous matrix	Variable	Pa s
η_f	Dynamic viscosity of the fluid phase (i.e. melt), spatially constant	Varied	Pa s

Table 1
Continued

Symbol	Definition	Value	Units
η_s	Effective shear viscosity of the porous matrix	Variable	Pa s
κ	Thermal diffusivity (equal for all rock types)	$0.923 \cdot 10^{-6}$	$\text{m}^2 \text{s}^{-1}$
λ	Thermal conductivity (equal for all rock types)	2.5	$\text{W m}^{-1} \text{K}^{-1}$
ρ	Mean density of the crustal rocks including melt	Variable	kg m^{-3}
ρ_f	Density of the fluid phase (i.e. melt)	Variable	kg m^{-3}
ρ_s	Density of the solid phase	Variable	kg m^{-3}
ρ_0	Reference density at reference temperature and pressure	2,700	kg m^{-3}
ρ_{enr}	Reference density of enriched solid	2,600	kg m^{-3}
ρ_{0f}	Reference density of granitic melt	2,300	kg m^{-3}
ρ_{dp}	Reference density of the depleted rock	3,100	kg m^{-3}
τ_{ij}	Viscous stress tensor in the solid phase	Variable	Pa
τ_{II}	Second invariant of the viscous stress tensor	Variable	Pa
τ_{max}	Depth dependent Byerlee-type maximum shear stress	Variable	Pa
φ	Volumetric melt porosity (i.e. melt fraction)	Variable	–
φ_{eq}	Equilibrium melt fraction	–	–

“enriched” (in SiO_2) for compositions near A and “depleted” (in SiO_2) for compositions near B. Compared to Schmeling et al. (2019), the melting law is improved by prescribing curved (“cigar shaped”) solidus and liquidus curves (Figure 1). Pressure dependence of melting is included by assuming depth-dependent solidus and liquidus curves as in Schmeling et al. (2019). Melt and solid are always in thermodynamic equilibrium (e.g., Ribe, 1985). While natural examples of such a binary solid solution phase diagram include olivine (fayalite to forsterite) as a constituent of mantle rocks, or feldspar (albite to anorthite) as a constituent of continental crust, our approximate phase diagram is used to mimic SiO_2 variations during melting of a typical meta-greywacke. We neglect complications due to multi-component melting which would also include eutectic melting. The composition varies between 0, representing full enrichment (granite), and 1, representing full depletion (granulites). The

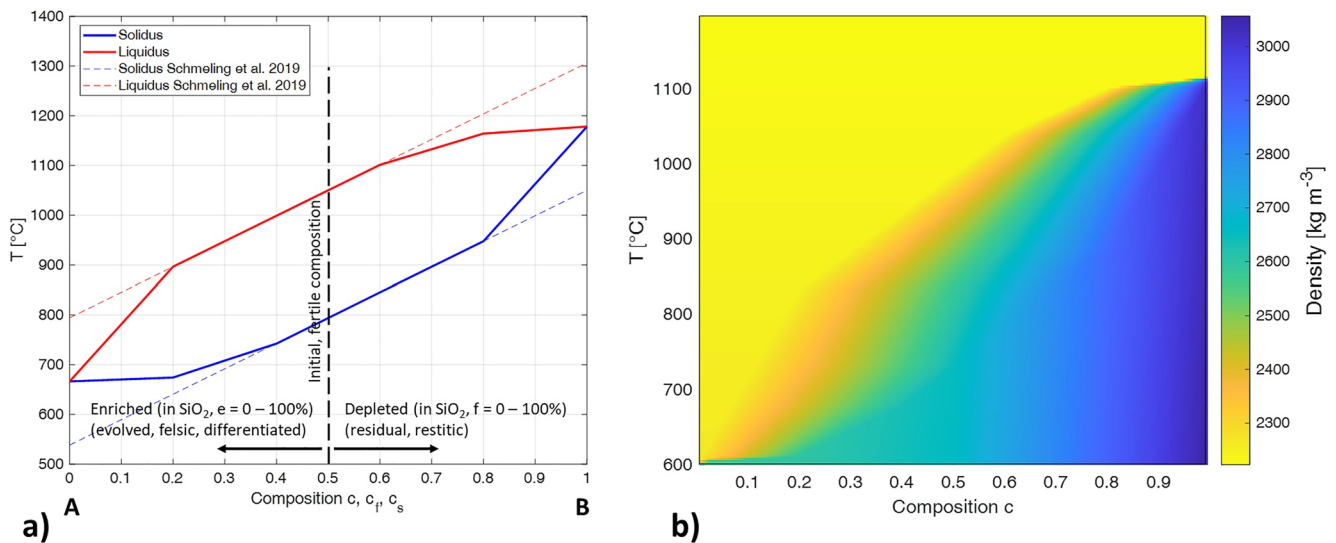


Figure 1. (a) Simplified phase diagram of a binary solid solution system with components **A** and **B** at pressure 0. **A** can represent a rock or magma with 75% SiO_2 and **B** a highly depleted residuum of meta-greywacke with 40% SiO_2 . For the initial fertile meta-greywacke, a SiO_2 component of 57.5% was assumed, which corresponds to $c = c_0 = 0.5$. The composition of melt and residuum was calculated using the lever-rule (see text and Schmeling et al. (2019)). Pressure dependence is included by assuming depth-dependent solidus and liquidus curves with a constant gradient of 2.334 K/km as in Schmeling et al. (2019). (b) Density map based on Equations 1–3 including the effect of temperature, melt fraction, and composition at zero pressure.

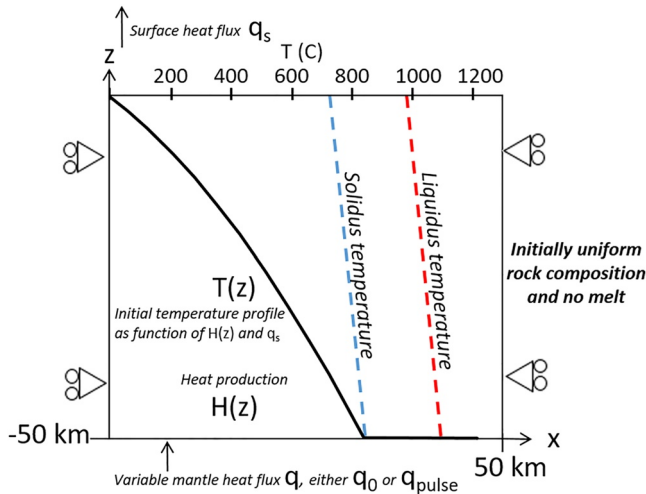


Figure 2. Model setup indicating the mechanical and thermal boundary conditions, the initial temperature profile and the depth-dependent solidus and liquidus temperature curves. The triangles with the circles near the box sides symbolize free slip boundary conditions.

initial (meta-greywacke) composition c_0 is assumed as 0.5. The approximated solidus and liquidus temperature in Figure 1 and their pressure dependence (Figure 2) were chosen in a way to generate a melting curve (degree of melt vs. temperature) for the initial $c_0 = 0.5$, which roughly resembles experimental curves for meta-greywacke (Clemens & Vielzeuf, 1987; Clemens, 2005; Li et al., 2022). The eutectic jump in melt fraction near the solidus temperature from a few % up to 20%, depending on water content, is neglected. It should be noted that our formulation could also be formulated in terms of an approximate eutectic phase diagram (Bittner & Schmeling, 1995), however, in the present formulation this would be numerically too expensive (see Appendix B).

The depletion f of the solid is defined as

$$f = \frac{c_s - c_0}{1 - c_0} \quad (5)$$

where c_s is the solid composition. Depletion is 0 as long as the solid has the initial composition, and it reaches 1 (= 100%) if the solid has the composition B, that is, $c_s = 1$. Similarly, the enrichment can be defined by $e = \frac{c_s - c_0}{-c_0}$ ensuring that $e = 1$ if the solid has the composition A, that is, $c_s = 0$. In other words, depletion is the relative deviation of c from the initial value 0.5 toward composition B, and enrichment toward composition A. The equilibrium melt fraction is given by the lever rule

$$\varphi_{\text{eq}} = \frac{c_s - c}{c_s - c_f}, \quad (6)$$

where c is the local composition of the solid-melt mixture,

$$c = (1 - \varphi)c_s + \varphi c_f, \quad (7)$$

and c_f is the melt composition. In the present formulation the lever rule is used for the non-linear liquidus and solidus curves, while in Schmeling et al. (2019) the dashed linear curves have been used (Figure 1). Melting and solidification are calculated by iteratively adjusting the solid and liquid compositions and the melt fraction to their equilibrium values including latent heat. At the same time the resulting melt and solid compositions are advected with the appropriate flow velocities of the melt and solid, respectively. The numerical formulation of this melting law is presented in Appendix B.

Following the arguments of Schmeling et al. (2019), we identify the composition $c = c_0 = 0.5$ (i.e., enrichment $e = 0$) with a SiO_2 content of 57.5% representative of the fertile meta-greywacke. Fully depleted rock becomes silica poor and granulitic. We assign 100% depletion (i.e., $c = 1$) to ~40% SiO_2 . To quantify the formation of granitic batholiths, we follow the classification for S-type granites with a SiO_2 content ranging from 63% to 75% (Chappell & White, 2001; Frost et al., 2001). Thus, identifying full enrichment (i.e., $c = 0$, $e = 1$) with 75% SiO_2 , the lower bound 63% SiO_2 for granitic rock correlates with an enrichment of $e_{\text{granite}} = 0.314$. Figure 2b shows the resulting temperature-, porosity-, and composition-dependent density map at zero pressure. From these considerations we can use the 2D-enrichment fields of our models to determine the size of the evolving and final SiO_2 -rich bodies which we call batholiths. The mean thickness of these bodies averaged over the width of the model ($h = 50$ km) is calculated by integration over the full area F of the model

$$h_{\text{bath}} = \frac{1}{h} \iint_F H(e(x, z) - e_{\text{granite}}) dx dz \quad (8)$$

where $H(\vartheta)$ is the Heaviside step function ($H(\vartheta) = 1$ if $\vartheta > 0$ or $H(\vartheta) = 0$ if $\vartheta \leq 0$).

The rock rheology is assumed independent of chemical composition, and represents wet quartz (Kirby & Kronenberg, 1987). See Appendix A for the equations and Table 1 for the chosen parameters. The porosity dependence of shear and bulk viscosity is taken as in Schmeling et al. (2019). Porosity impacts on the viscosities

causing a drop from the intrinsic values of wet quartz to almost zero at porosities close to 0.5, and at higher porosities an exponential lower truncation viscosity is assumed (see Schmeling et al. (2019) for more details and the assumed values). The melt viscosity is assumed constant, its actual value enters indirectly by the parameter combination d^2/η_f (see previous section) which is prescribed by the retention number. To recalculate d^2/η_f from a given retention number the assumed model height h of 50 km and the scaling viscosity η_0 of 10^{20} Pa s have to be used. The retention number in most models is 3, but for exploring the parameter space it is varied between 1 and 100. Given this range, values of the melt viscosity range between $0.4 \cdot 10^3$ Pa s for $d = 1$ mm and $Rt = 1$, to $0.4 \cdot 10^{13}$ Pa s for $d = 10$ m and $Rt = 100$ (see also the discussion in Schmeling et al. (2019)). Spacings of anastomosing leucogranitic sheets forming pathways through partially molten rocks of 5 m have been observed by Symington et al. (2014).

The density of undepleted rock at surface temperature is assumed as $\rho_0 = 2,700$ kg/m³, it varies linearly to $\rho_{dp} = 3,200$ kg/m³ for fully depleted residual rock (granulite) or to $\rho_{enr} = 2,600$ kg/m³ for fully enriched rock (solid granite). When exploring the parameter space, ρ_{enr} is varied to values as low as $2,300$ kg/m³, while the melt density is fixed to $\rho_{of} = 2,300$ kg/m³ throughout the paper. With these densities, we note that the limiting 10% density variations required for the Boussinesq approximation are exceeded when locally the melt fractions, depletion or enrichment exceed 54%. In other words, local volumes of magma bodies or granitic batholiths with more than 54% melt fraction or enrichment, respectively, are underestimated by about 10%, while volumes of highly depleted material are overestimated by about 10%. When defining batholith or depleted volumes we integrated over larger regions which minimizes such errors to only a few %.

The pre-factor of the permeability-porosity relation, d^2/C , is chosen implicitly by the retention number. Other physical parameters such as the thermal conductivity, heat capacity c_p , thermal expansivity, depth dependent radiogenic heat generation rate, latent heat L , exponent of the porosity-permeability relation n_ϕ are the same as in Schmeling et al. (2019). Most of them are given in Table 1.

2.3. Model Layout

Our 2D model aims to represent a magma system in thickened continental crust with a crustal thickness in excess of 50 km (Zandt et al., 1994). The bottom of the model (Figure 2) represents a depth at which heat is added by magmatic underplating from the mantle, thus the Moho is assumed to be below 50 km. The horizontal size of 50 km with reflective mechanical and thermal boundary conditions allows a total horizontal extent of 100 km, which is about half the width of Altiplano. At top and bottom, non-flexible free slip boundary conditions are assumed, representing low viscosity material above (air) and below (magmatic underplating) the model box. At the top, the temperature is fixed at 0°C, at the bottom, a laterally constant heat flux is assumed which may vary with time. Boundary conditions for the solid and melt phases are no influx or outflux at all boundaries. The initial temperature profile has been chosen to represent an unmolten crust, that is, it is subsolidus down to 50 km depth where the depth-dependent solidus temperature is exactly reached. This is done by calculating a conductive temperature profile with depth-dependent radiogenic heating with the parameters used in Schmeling et al. (2019) but adjusting the bottom heat flux to a value of $q_0 = 29.5$ mW/m² resulting in a bottom temperature just at the solidus temperature (845°C). A sinusoidal lateral temperature perturbation of 10 K is added to the initial temperature field to initiate dynamic behavior in the model. To mimic magmatic underplating, a bottom heat flux condition is assumed with a single elevated pulse $q_{pulse} = 84$ mW/m² over a time period of t_{max} of 10 Ma, or a series of three successive heat flux pulses with values of 120 mW/m² during time intervals of t_{pulse} of 2 Ma length with intervals of 2 Ma of normal conditions in between. The total (time integrated) heat energy input at the base of the crust in J/m² is given by $Q_{tot} = t_{max}q_0 + Nt_{pulse}(q_{pulse} - q_0)$, where N is the number of pulses. It is identical for both models. To explore the parameter space, the values of the heat pulses are varied between 48 to 96 mW/m² for the single pulse models and 60 to 140 mW/m² for the multiple pulse models, always keeping the total heat energy the same for single and multiple pulse experiments. The governing equations (Appendix A and B) are solved by finite differences with the code FDCON (e.g., Schmeling et al., 2019 and references therein).

Given the excess heat flow over the duration of each heat pulse, the equivalent thickness of a molten basalt layer can be calculated by accounting for the latent and sensible heat of such a layer:

$$h_{bas} = \frac{(q_{pulse} - q_0)t_{pulse}}{\rho_{bas}(L_{bas} + c_{pbas}(T_{bas} - T_0))} \quad (9)$$

Here q_{pulse} is the heat flux of the heat pulse of duration t_{pulse} , q_0 is the initial or background heat flux, ρ_{bas} , L_{bas} , c_{pbas} , and T_{bas} are the density, latent heat, heat capacity, and temperature of the underplating basalt, respectively, and T_0 is the initial bottom temperature (equivalent to the steady state bottom temperature for a bottom heat flux of q_0). Using typical values for molten basalt, 2 Ma long heat pulses from 60 to 140 mW/m², results in underplating layers equivalent to 0.7–2.6 km thickness, respectively. These thicknesses must be multiplied by 3 for the total of 3 pulses over 10 Ma or the equivalent single 10 Ma long pulse, resulting in total underplating thicknesses of 2.1–7.8 km for the heat fluxes mentioned above.

3. Results

3.1. Two Typical Models Showing Batholith Emplacement and Convective Recycling Modes

First, we show the general behavior of melt differentiation and ascent in our models and identify the two main modes batholith emplacement and convective recycling. We define a reference model setting with a retention number of 3. We assume either a single heat pulse of 84 mW/m² over a time period of 10 Ma or multiple heat pulses of 120 mW/m² of 2 Ma duration each. We ran these models (and all others) for 14 Ma years. Figure 3 shows a temporal series of the results (see also Movies S1, S2, S3, S4, S5, and S6 in the Supplementary Material).

In the single heat pulse model, a thin partially molten layer forms near the bottom shortly after onset of heating. As the melt fraction increases with time, two-phase flow allows for melt segregation and a thin melt accumulation layer (>50% melt) forms on top of the progressively thickening partially molten layer. This layer breaks up into diapirs after 0.797 Ma (Figure 3a, uppermost row, 0.797 Ma), or more precisely, into partially molten rising plumes or mush bodies which start freezing at their top. It is noteworthy that there are two processes running in parallel: the *en masse* mush rise in the diapirs and the relative motion between melt and solid through the interstices. In this example at 6 Ma the velocity of the melt within the core of the diapir is about 30% faster than the rise of the surrounding solid mass. Two well-developed convection cells form with two mature partially molten hot plumes in the upwelling parts which rise to 22 km in 10 Ma and one cold unmolten downwelling limb in the center of the figure near $x = 25$ km. The third row of Figure 3a shows the temperature distribution of this convection pattern. This convection is essentially driven by melt and thermal buoyancy and can be referred to as phase-change-driven convection. After switching off the heating at 10 Ma, convection continues, persisting as partially molten mush bodies for at least past 14 Ma, but as the melt gradually freezes the convective vigor decreases. Focusing on composition c (second row), results show the evolution of large bodies with $c < 0.5$ indicating that they are enriched in silica (light blue), while a depleted layer with $c > 0.5$ (yellow) grows to a final thickness of ~ 4 km at the bottom. The tops of melt-rich diapirs are clearly enriched (yellow structures at 0.797 Ma). Upon freezing, the enriched regions lose some of their buoyancy and are sheared and incorporated into the downwellings (faint bluish rims around the wide green cells at 2 Ma and later). This remixing of enriched material into the downwellings will be referred to as **mode of convective recycling**. Parts of the depleted bottom layer are entrained into the rising plumes (e.g., light yellow central cores in the plumes at 4 Ma) (e.g., Chappell et al., 1987; Cruden et al., 1995). Due to this entrainment, the melting temperature locally increases within the rising plumes accompanied by reduced melt fractions in the center of plumes. Furthermore, the increased depletion within the plumes leads to reduced buoyancy. This leads to splitting of the plumes, which is most pronounced when the plumes rise at the sides of the model box where symmetrical boundary conditions fix the position of the plumes. We may call such plumes “low melt-fraction-core plumes,” labeled in Figure 3a (see also the Movies S1, S2, S3, S4, S5, and S6 in the Supplementary material). Such plumes transport depleted material upwards into the shallower regions reducing the average enrichment there. Thus, despite a general trend toward a crustal stratification comprising depleted material below and enriched above, we observe both, convective downward recycling of enriched material and upwards recycling of depleted material.

The evolution of the model with three heat pulses shows a stark contrast (Figure 3b). The higher heat pulses (120 mW/m²) lead to stronger partially molten diapirs/plumes, larger segregation velocities \bar{v}_{gr} , that is, larger differences between melt and solid velocity. Melt accumulates in melt-rich caps reaching further up (0.668 Ma). During the first heat pulse these caps widen and freeze, and enriched material is remixed back into the lower crust (wide areas of light bluish material within the downwellings). Switching off the heat pulse at 2 Ma leads to the melt fraction dropping to almost zero. However, plumes are still warm and attract the new pulses of rising melt generated during the second and third pulse. At the end of the second pulse the melt within the mushy diapir rises $\sim 40\%$ faster than the surrounding solid mass. Melt accumulates (melt fraction >50%) at the top of the mushy

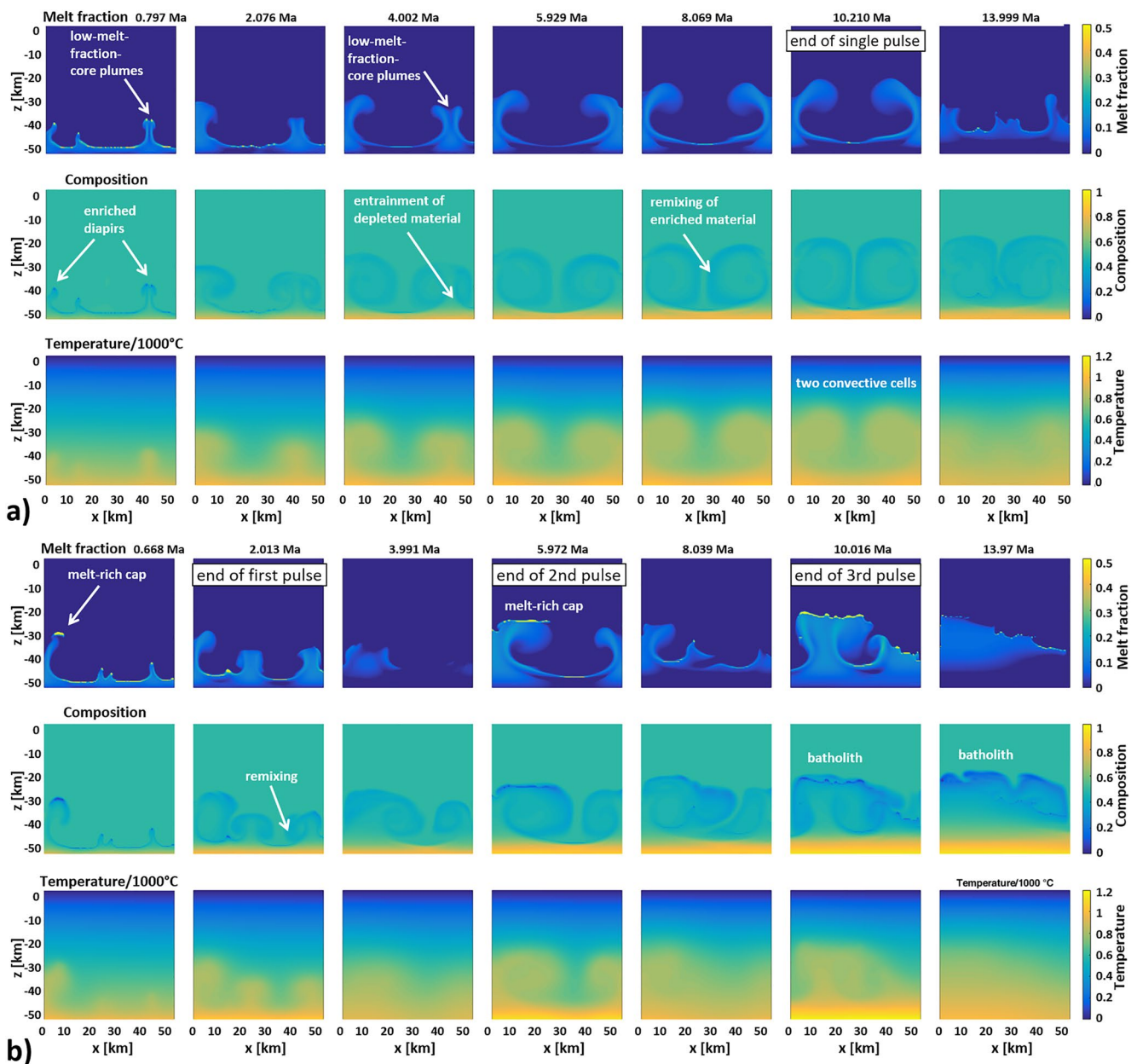


Figure 3. Temporal evolution of melt fraction, composition, and temperature for a model of a fertile, 50 km thick crust where a sudden heat input from below leads to melting and melt ascent with chemical differentiation. (a) Single heat pulse of 84 mW/m² over a time period of 10 Ma, (b) multiple (three) heat pulses each with a duration of 2 Ma, a time interval of 2 Ma between the pulses and an amplitude of 120 mW/m²; retention number, *R_t*, is 3 and enrichment solid rock density is 2,600 kg/m³. High resolution movies of the temporal evolution are also available in Movies S1, S2, S3, S4, S5, and S6.

plumes, forming potentially eruptible melt-rich caps. These caps form on top of plumes which do not contain as much depleted material as those in Figure 3a, that is, the plumes in Figure 3b evolve into less pronounced “low melt-fraction-core plumes.” This is because the more intense bursts of melting lead to more intense differentiation and density contrasts: more enriched material is more buoyant resisting recycling, while more strongly depleted material at the base are denser resisting being dragged up. During the second and third pulses, less enriched material (both melt and frozen material) is recycled back than during the first pulse, and less depleted material is entrained into the rising plumes. This leads to the accumulation of melt-rich caps at the top of the plumes that merge into batholiths of enriched material (blue layers in the composition field at 10 and 14 Ma). This enriched silicic body is irregular in shape and distribution because it is a result of the gradual aggregation of several small melt-rich diapirs that enter previously enriched regions and that may solidify at different depths. This

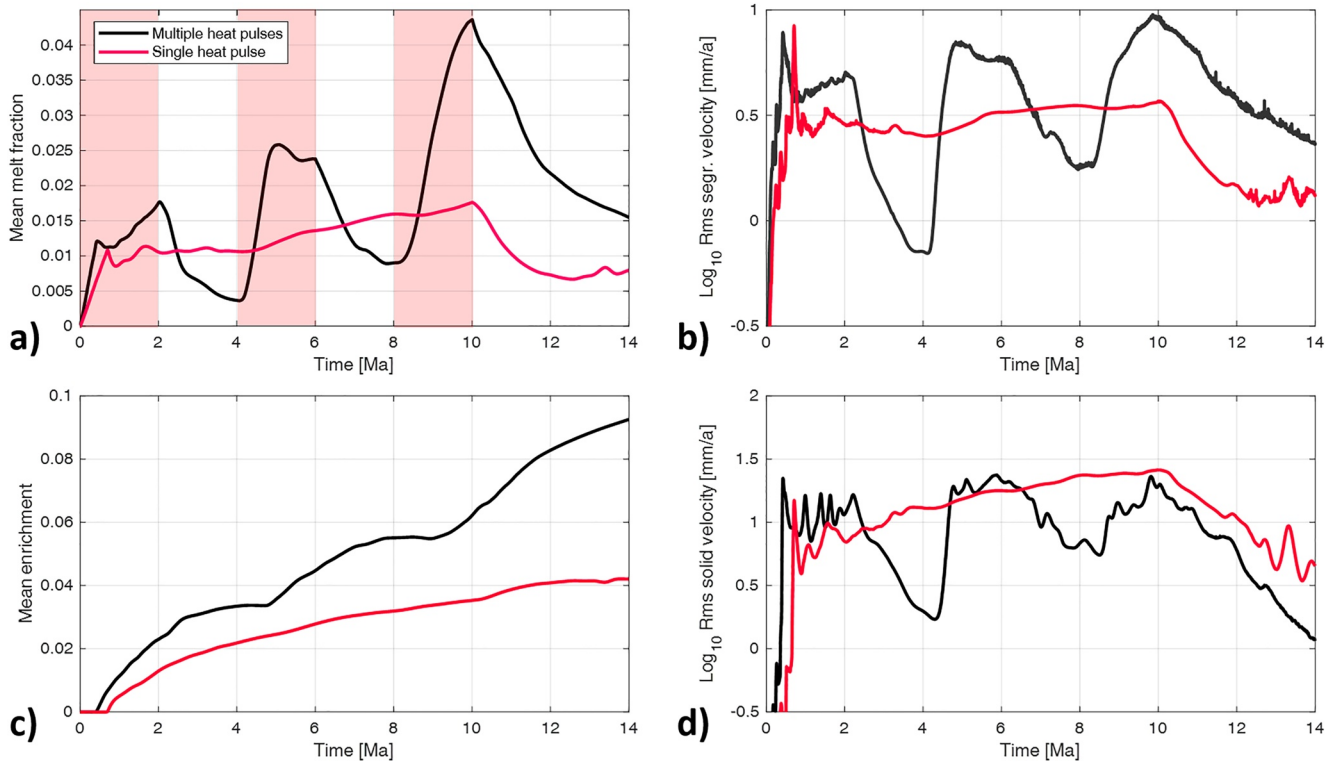


Figure 4. Evolution of the models in Figure 3. (a) Mean melt fraction, (b) root mean square (RMS) of segregation velocity (i.e., the difference between melt and solid velocity), (c) mean enrichment, and (d) RMS of solid velocity as a function of time. Pink columns in panel (a) indicate the duration of heat pulses for the model with multiple pulses.

accumulation into an enriched layer will be referred to as the *mode of batholith emplacement*. Another example clearly depicting the two modes is shown and discussed in Appendix D, Figure D3.

Figure 4 compares global key quantities of the single and multiple pulse models. These parameters include the spatially averaged melt fraction, enrichment, solid velocity, and segregation velocity \bar{v}_{sgr} that is, the difference between melt and solid velocity. The means of the velocity vector fields were obtained by taking the *square root* of the spatial *mean* of all *squared* vector components, that is, the *root mean square* (RMS) velocities. Although the total heat input is the same, on average three pulses generate more melt than a single pulse (Figure 4a). The mean enrichment increases to twice the value of the single pulse model (Figure 4c) because each pulse leads to more intense melting (Figure 4a) facilitating faster melt migration (Figure 4b), forming enriched caps, which are less effectively recycled back into the lower crust. The RMS velocity of segregation of the multiple pulse model is higher on average and particularly during and after the third pulse (Figure 4b). This leads to the formation of a batholith instead of convective recycling. The RMS of the solid velocity of the single pulse model is essentially faster (Figure 4d). This is typical for the convective recycling mode in Figure 3a in contrast to the batholith emplacement mode of Figure 3b and will be discussed in more detail in Section 4.1.

We now focus on the evolution of the thermal structure of the two models in Figures 3a and 3b (bottom rows). In the single pulse model, after 4 Ma two spatially persistent convection cells with growing hot plumes and cold downwellings develop. In contrast, in the multiple pulse model each new pulse reorganizes the temperature field and the number and shapes of plumes and after 10 Ma essentially one plume dominates the thermal field. Lateral temperature variations reach up to 220 K at 10 Ma in both models. Figures 5a and 5d show the characteristic temperature profiles at 10 Ma for the two models. The profiles are taken at the x -positions where the vertically averaged temperatures are largest (red curves) or smallest (blue curves), respectively, and the positions are indicated in the legends. Comparison of the hot profiles for the single and the multiple pulse cases shows that the hot plume of the multiple pulse model reaches shallower crust and melt is present to 20–25 km depth compared to 25–30 km in the single pulse case. However, this is only an apparent difference because inspection of the full 2D temperature field (Figure 3a at 10 Ma) reveals that the single pulse plume also reaches the same shallower

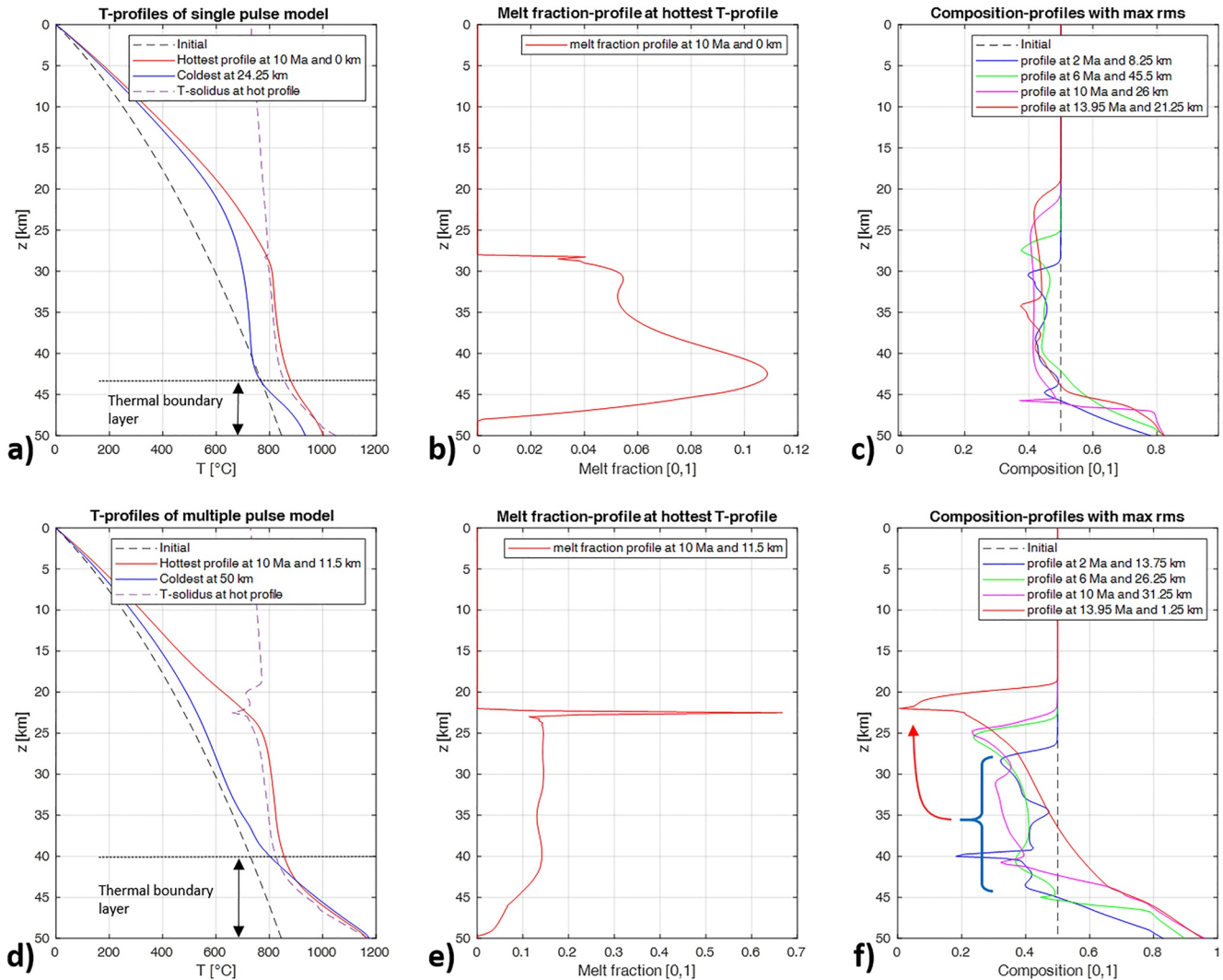


Figure 5. Vertical profiles of (a, d) temperature and solidus temperature, (b, e) melt fraction, and (c, f) composition at specific times and position indicated in the legends. “Hottest” and “Coldest” profiles are defined by taking the vertical average of temperature at all x -position and choosing those x -positions with the highest or lowest average temperatures, respectively. Upper row: single pulse model, lower row: multiple pulse model. In panel (f), the red arrow indicates that, with progressing time, enriched compositions are transported upwards and accumulate in an enriched batholithic layer at 22 km depth. Results are for the models in Figure 3.

depths 20–25 km but this is displaced horizontally in relation to the hottest vertical position in Figure 5d. The most important difference between the single- and multiple-pulse models is the thickness of the lower thermal boundary layer: about 7 km in the single pulse model and 10 km in the multiple pulse model. The thicker thermal boundary layer results from the thicker compositional depleted layer (Figures 5c and 5f), which is stagnant and does not take part in the convection. This difference in thermal boundary layer thickness results in a thinner central convection layer in the multiple pulse model with smaller convection velocities (and smaller RMS flow velocities, black curve in Figure 4d) resulting in a less effective vertical heat transport. Consequently, the surface heat flux in the single pulse model exceeds that of the multiple pulse model at times >9 Ma (Figure 6a).

In Figures 5c and 5f the composition profiles are shown at different times. Since the single pulse model is dominated by convective recycling, the composition within the convective zone is reduced only slightly from 0.5 to between 0.4 and 0.45 (Figure 5c). The corresponding melt fractions are small (mostly less than 10%) or even zero in the uppermost enriched part (Figure 5b). In contrast, the multiple pulse model is dominated by compositional differentiation, focusing melt and enriched rocks into a highly enriched batholith (c close to 0) fed by melt segregation from a wide melt-rich mush zone between 23 and 45 km depth (Figure 5e). This mush zone is responsible for providing a pathway and a source of melt out of the progressively depleted layer (c up to 0.9) underneath (Figure 5f). The end result is that the multiple pulse model has a much more strongly differentiated crustal profile.

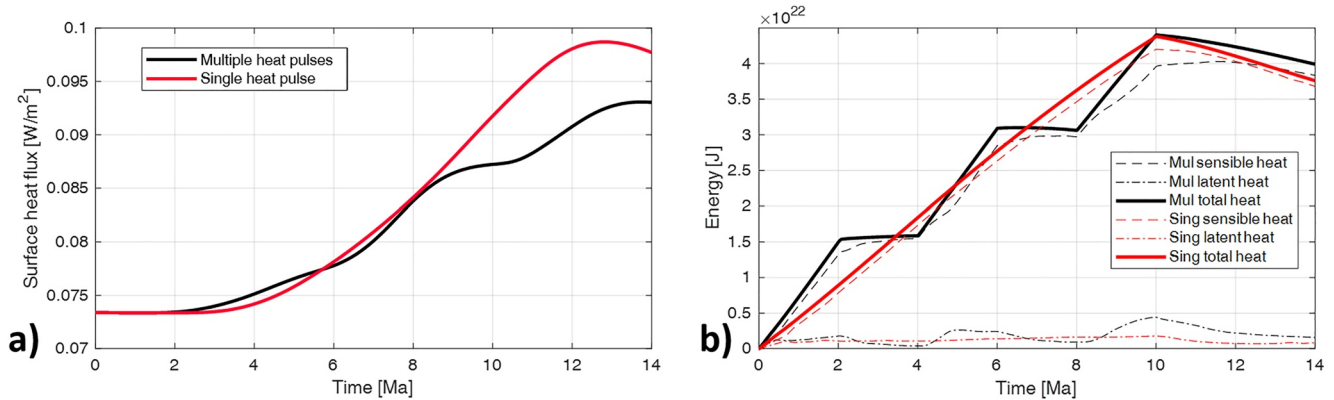


Figure 6. Thermal evolution with time of the two models. (a) Horizontally averaged surface heat flux. (b) Evolution of total heat content of the models. Total heat (bold curves) and the contributions due to sensible (dashed) and latent (dash-dotted) are shown. All energies are calculated assuming a $50 \times 50 \times 50$ km crustal volume.

This compositional differentiation leads to spatial variations of the solidus and liquidus temperatures that depend on c , the rock composition (c.f. Figure 1 for the dependence of the solidus temperature on composition). In Figures 5a and 5d, we have also plotted the depth- and c -dependent solidus temperatures (dashed lines). Interestingly the actual temperatures within the hot plumes are sub-parallel to the solidus temperatures, exceeding them by a few 10s K. In the multiple pulse model, both in the cold and hot columns the temperatures within the depleted stagnant conductive layer are also above solidus (Figure 5d) (note that within the depleted layer the solidus is approximately the same in the hot and cold regions). In contrast, in the convective recycling model the temperatures in the bottom thermal boundary layer are colder and lie below the solidus.

For a better understanding of the higher melt fractions and crustal differentiation of the multiple pulse case compared to the single pulse model, Figure 6b shows the evolution of the heat content of both models. During the first half of the heating time, that is, until 5 Ma, the multiple pulse model gains heat earlier and more rapidly than the single pulse model. Thus, more melt is created increasing crustal differentiation even though the total heat content is equal in both cases. During the second half (5–10 Ma) the heat supply of the multiple pulse model is delayed becoming steep at the end. Until 8 Ma the heat supply of the single pulse model is higher and because of its less differentiated crust, the convection is stronger, as well as the vertical heat transfer and the convective remixing. As expected after 10 Ma the total heat content of the two models is approximately the same, but for later times the stronger convection in the single pulse models increases the total cooling rate associated with a higher surface heat loss (Figures 6a and 6b). Because the total amount of melt is always smaller than 4% (c.f. Figure 4a), the fraction of energy stored in latent heat is always small compared to the contribution of total sensible heat (Figure 6b, dash-dotted vs. dashed curves). In the case of the multiple pulse model, the maximum amount of melt and stored latent heat is reached at 10 Ma, its subsequent release at shallow depths contributes to the surface heat flux by ~ 6 mW/m², marked by an increase after 10 Ma (Figure 6a, black curve).

The single or multiple pulse models show that for the same average heat input the results are completely different. We thus tested three-pulsed cases with the same total heat input but with decreasing, identical or increasing heat flux amplitudes (Figure 7). These three cases show significantly different behaviors: the decreasing heat pulse case shows important recycling, while constant or increasing heat pulses result in batholith formation. To explain the results, we conjecture that the first strong heat pulse (140 mW/m²) of the decreasing heat pulse model already generates small melt-rich caps leading to a localized thin layer of enriched material at ~ 25 km depth. The subsequent weaker pulses (120 and 100 mW/m²) generate plumes with smaller melt fractions than the first pulse, but entrain more depleted material from the bottom, left over after the first pulse. As a result, these later plumes are pronounced “melt-poor core plumes” with only small amounts of melt within melt-rich caps. Thus, almost no accumulation of enriched material to form batholiths happens. The remnant of a thin enriched layer formed at 10 Ma is visible at $x = 32$, $z = -20$ km in Figure 7a whereas most of the enriched material has been recycled and forms a contorted blue band at depth. In contrast, the other two models generate more melt from pulse to pulse (Figure 7c) and entrain less depleted material within the plumes, that is, there are no “melt-poor core plumes.” As a result, they contain higher fractions of melt allowing for faster segregation during the second and third pulses (Figure 7c) while the solid plume velocities remain the same (Figure 7e). Melt accumulates within melt-rich caps, forming significant bodies of enriched material when freezing.

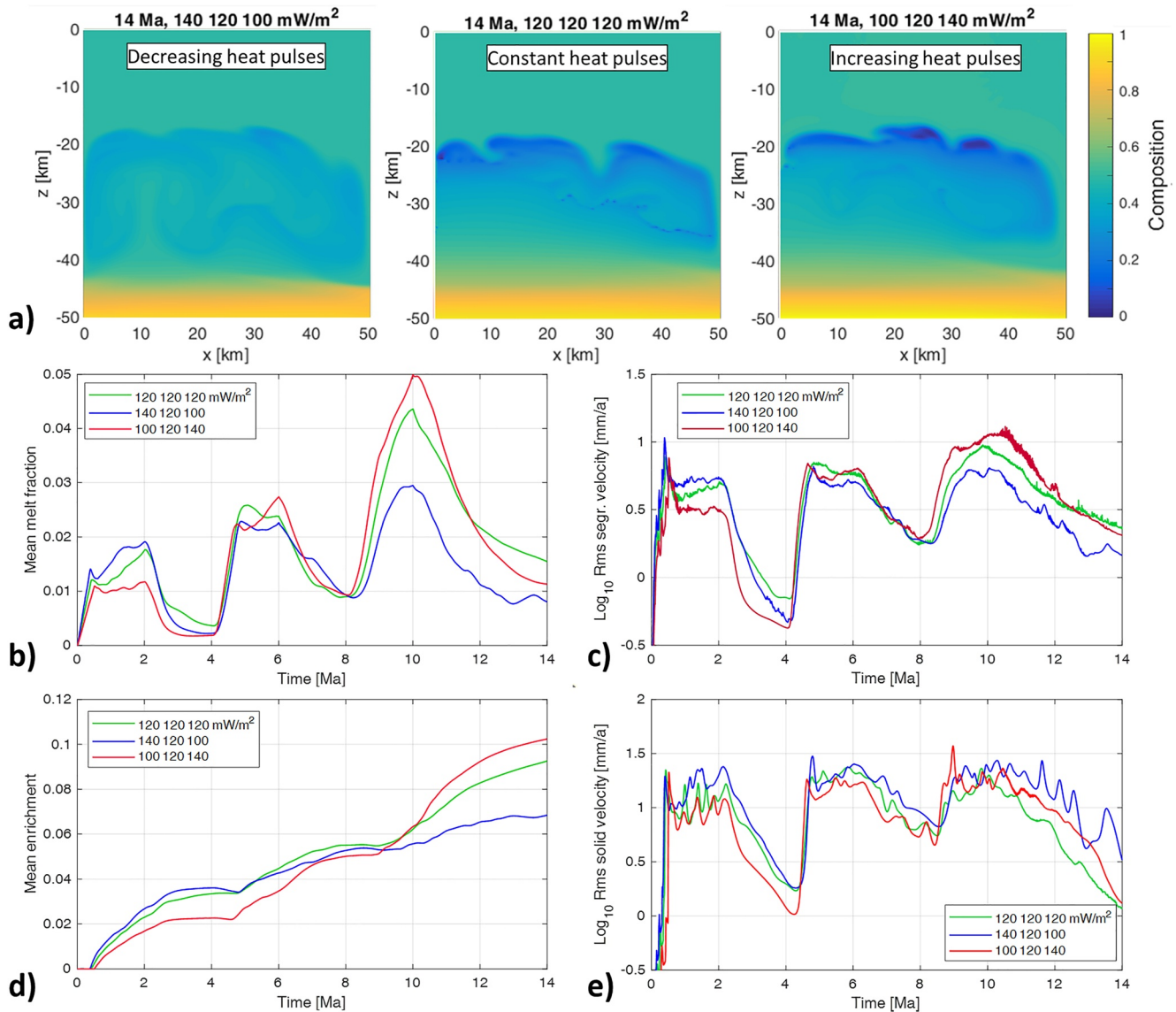


Figure 7. Effect of changing heat flux amplitudes systematically. (a) Final stage (after 14 Ma) of the composition fields for decreasing heat pulses (140, 120, and 100 mW/m²) (left), three consistent heat pulses of 120 mW/m² (center); and increasing heat pulses (100, 120, and 140 mW/m²) (right). (b) mean melt fraction, (c) root mean square (RMS) of segregation velocity, (d) mean enrichment, and (e) RMS of solid velocity as a function of time.

3.2. Effect of Varying Melt Mobility

Melt segregation strongly depends on the viscosity of the melt and on the permeability of the solid rock, that is, on the retention number Rt . A high retention number corresponds to immobile melts, which are retained in the matrix. To investigate its effect, we use the same model layout as above (Figure 3, Section 3.1). The retention numbers are set to 1, 3, 10, 30, and 100. From Section 2.2, such retention numbers are related to melt viscosities between 10^3 and 10^{13} Pa s, depending on the porosity length scale. Figure 8 shows the late-stage composition fields of the single- and multiple-pulsed models, but see also the full time evolution in Movies S7, S8, S9, S10, S11, and S12 available in the Supplementary material. For both series, the models with the highest melt mobility, $Rt = 1$, show strong segregation with extensive formation of enriched batholiths at around 20 km depth (blue regions) and strongly depleted lower crusts (yellow layers). Increasing Rt to 10 or higher, in both series, melt segregation becomes less important and the results are dominated by recycling. At $Rt = 100$, high melt viscosity inhibits segregation to such extent that batch melting dominates the phase-change-driven convection. This means that the upwelling limbs of the convection cells consist of partially molten mushes with relatively high melt fractions

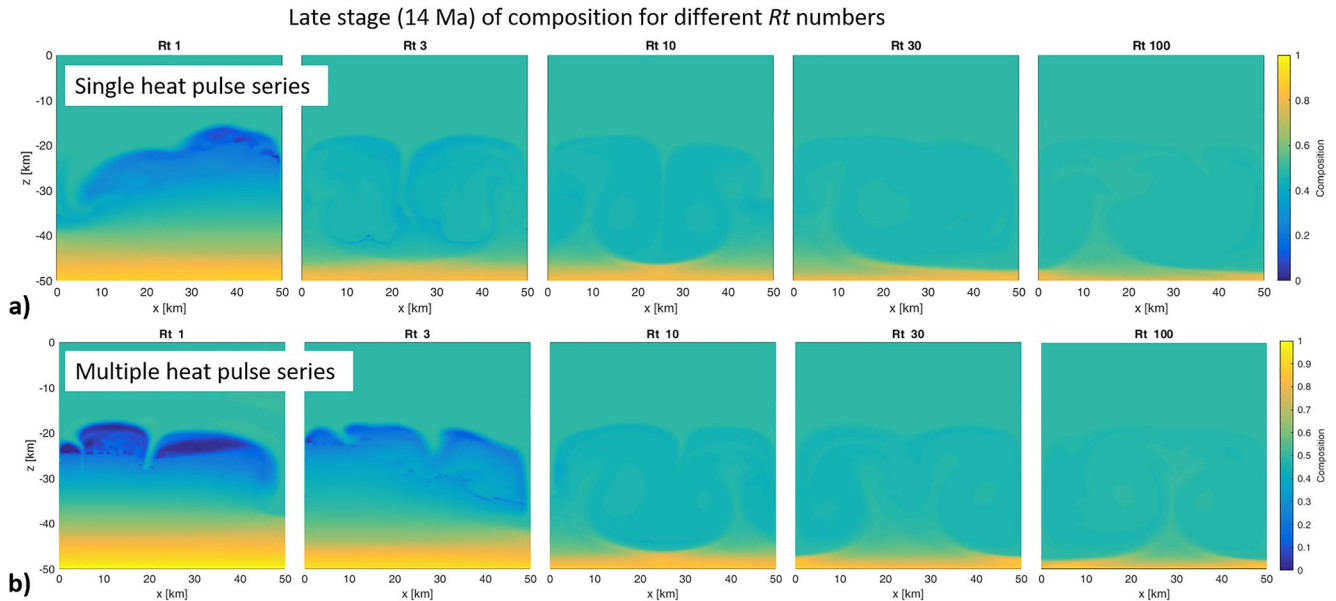


Figure 8. Composition at late stage (14 Ma) for different retention numbers Rt . (a) Upper row shows the models with a single heat pulse of 10 Ma duration, (b) lower row shows the multiple heat pulse models with three equal heat pulses, and with equivalent total heat input. High resolution movies of the full time evolution of the composition for models $Rt = 1, 3, 10$ are available in Movies [S7](#), [S8](#), [S9](#), [S10](#), [S11](#), and [S12](#).

($O(10\%–30\%)$) contributing to the plume buoyancy while the cold downwellings are essentially solid, due to melt crystallization without its segregation. This means that convecting rock volumes undergo several melting—solidification—remelting cycles without differentiation. At high Rt , melt segregation near the bottom is slow but still strong enough over 14 Ma to form a thin depleted layer (Figure 8, cases on the right). For the multiple pulse case, the change in mode from batholith accumulation to recycling occurs at $Rt > 3$ whereas it is between 1 and 3 for the single pulse case.

To study this transition in more detail, Figures 9 and 10 show the time-dependent evolution of a few key parameters of the single and multiple pulse models, respectively. Figures 9a and 10a show the mean enrichment. The batholith emplacement mode ($Rt = 1$ for both heating cases, $Rt = 3$ only for the multiple case) correlates with pronounced increases of mean enrichment up to 0.10, while the recycling mode is characterized by weak increases of mean enrichment up to 0.04. Figure 9c shows that first the amount of melt increases linearly and equally for all Rt values. During this stage, melt may already segregate within the thin layer near the bottom or stay within the matrix in the models with high Rt . In both cases the same amount of melt is generated and freezing has not yet started as long as the enrichment curves in Figure 9a are still equal to zero. Only after the rise of plumes and subsequent melt segregation and accumulation within melt-rich caps, melt starts to freeze in the upper crust. At this time the mean melt fraction curves depart from the initial linear trends. Due to high melt mobility, this happens much earlier for the low Rt models. As a result of reduced segregation, most melt is retained in the $Rt = 100$ model. The $Rt = 1$ model (Figure 9c) does not follow this trend of melt fraction decreasing with decreasing Rt . This deviation can be explained by the continuous formation of an enriched region between 15 and 30 km (Figure 8a, $Rt = 1$) which effectively reduces the solidus curve in that region and leads to melts reaching 20 km depth (at 10 Ma). In contrast, the $Rt = 3$ model (Figure 8a, or Figure 3a) is associated with pronounced remixing convection and thus less enrichment and higher solidus temperatures at >20 km depth. Thus, the $Rt = 3$ model has smaller melt fractions. The effect of reduction of melt mobility is clearly seen in the RMS melt segregation velocity (Figure 9b) that increases with decreasing Rt . However, the RMS solid velocity of all models with $Rt > 1$ (Figure 9d) evolves similarly (except for the times of onset of diapiric rise). This is noteworthy in view of the mean melt fraction which differ by up to a factor 3. Checking the models in detail (not shown) reveals that the different sources of positive and negative buoyancy (thermal, melt, entrained enriched or depleted material within downwelling or upwelling, respectively) combined with the lower viscosity of the warmer $Rt = 100$ model, indeed compensate each other and result in similar overall solid velocities (Figure 9d). In the model with batholith formation ($Rt = 1$) the thickness of the convective layer becomes smaller with time reducing the RMS solid velocity.

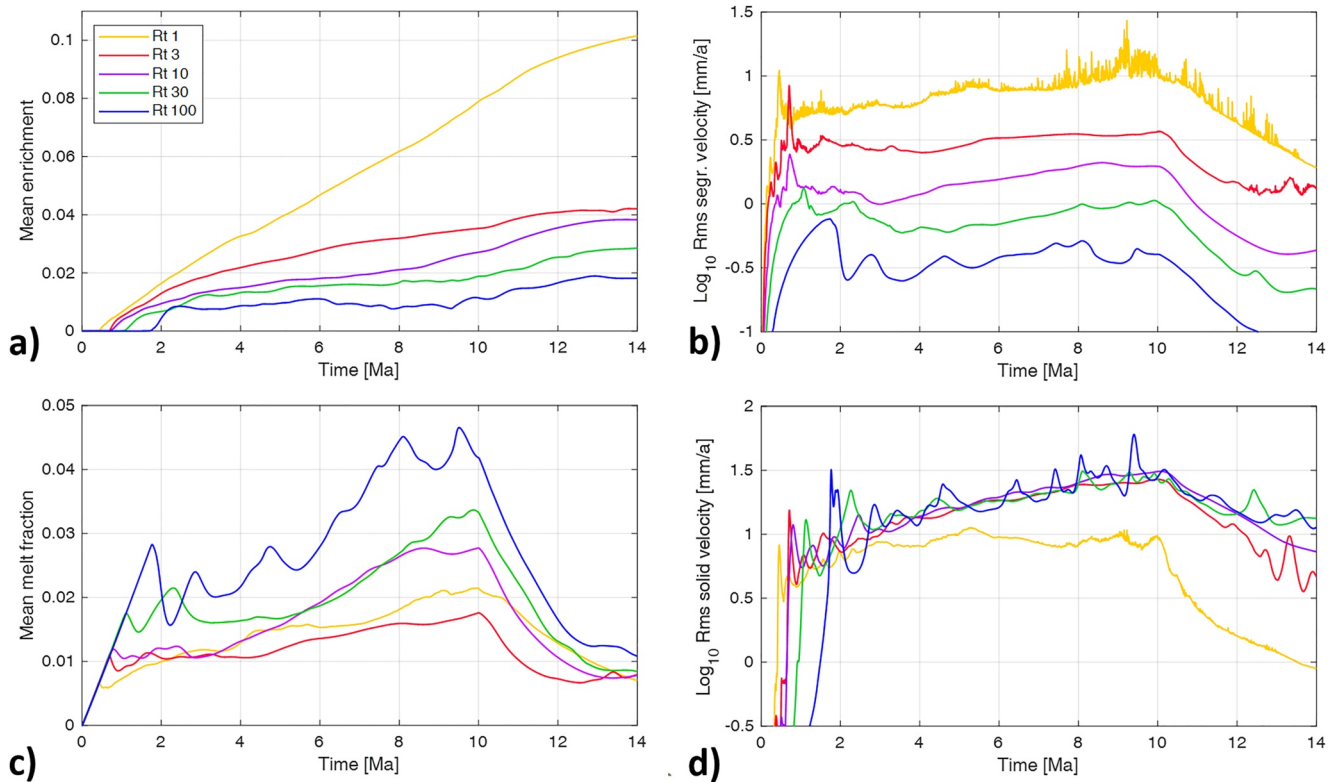


Figure 9. Effect of different Rt numbers ($Rt = 1, 3, 10, 30,$ and 100) for the single heat pulse case on enrichment (a), root mean square melt segregation velocity (b), melt fraction (c), and solid RMS-velocity (d) versus time. Bottom heat flux is increased to 84 mW/m^2 for 10 Ma.

Figure 10 shows similar curves for the model with the three heat pulses. Clearly, the mean enrichment curves for $Rt = 1$ and $Rt = 3$ (Figure 10a) significantly depart from the other curves indicating effective formation of enriched magmatic bodies. The correlation between mean melt fraction and Rt is only clearly observed during the first two pulses (Figure 10c). When the third pulse occurs, in case of low Rt larger amounts of enriched material have already accumulated at shallow depth and have solidified. This enriched material has a lower melting temperature and melts when the front of the third heat pulse reaches shallow depth, increasing the melt fraction to values comparable or above the values of the retained melt in high Rt cases.

Switching off the heat pulse leads to a clear decrease in RMS solid velocity only after the first pulse, while after the second and third pulses the decrease is much less pronounced (Figure 10d). We explain this by some transient behavior in establishing phase-change-driven convection: while after the first pulse not enough heat and melt is available to drive convection by phase change, after the second and third pulses enough melt and heat is present so that continuous phase-change-driven convection takes over. A similar observation can be made for the segregation velocity. Both models with batholith formation ($Rt = 1, 3$) keep high segregation velocities during and after the third pulse, while solid velocity (diapiric velocity) drops steeply.

3.3. Effect of Varying Heat Flow

In this section the effect of the magnitude of heat input is studied both for a single and for multiple heat pulses with retention number of 3. Again, the total amount of heat input in the single and multiple pulse models is the same for 10 Ma. Figure 11 shows the composition fields after 14 Ma. A weak single heat pulse of 48 mW/m^2 leads to some melting and weak diapiric rise with some segregation up to a depth of 30 km. Convection is only weakly supercritical, both the RMS solid and segregation velocities are slow, of order 1–2 mm/a (Figures 12b and 12d). The actual velocities are so slow ($O(4 \text{ mm/a})$) within the lower partially molten crust (30–45 km) that during 10 Ma no multiple overturns are possible to remix enriched material back into the crust. As a result, batholith emplacement of enriched material is visible near the top of the melting zone at 30 km depth (Figure 11a, left).

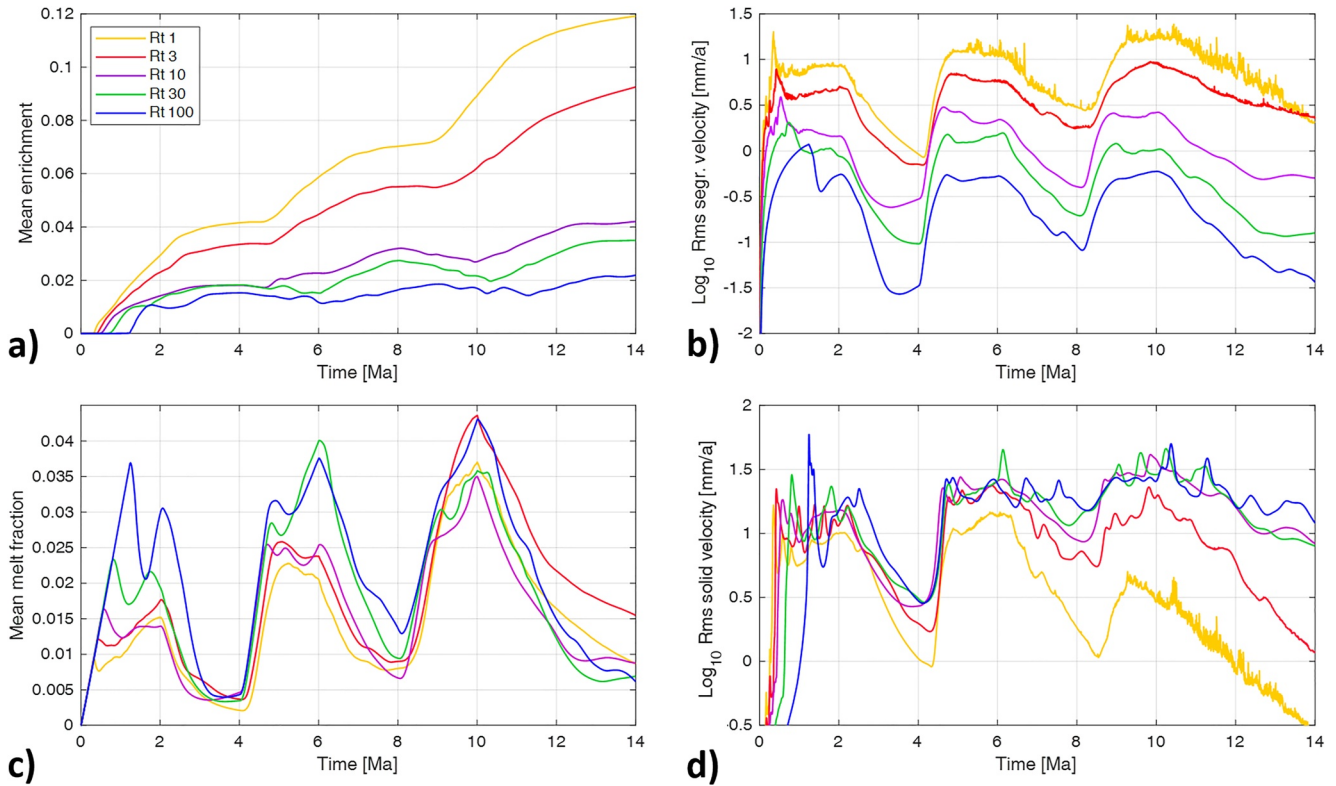


Figure 10. Effect of different Rt numbers ($Rt = 1, 3, 10, 30,$ and 100) for the multiple heat pulse case on the enrichment (a), root mean square (RMS)-melt segregation velocity (b), melt fraction (c), and solid RMS-velocity (d) versus time. Bottom heat flux is increased to 120 mW/m^2 for three successive heat pulses with a duration of 2 Ma each and a time interval of 2 Ma between pulses.

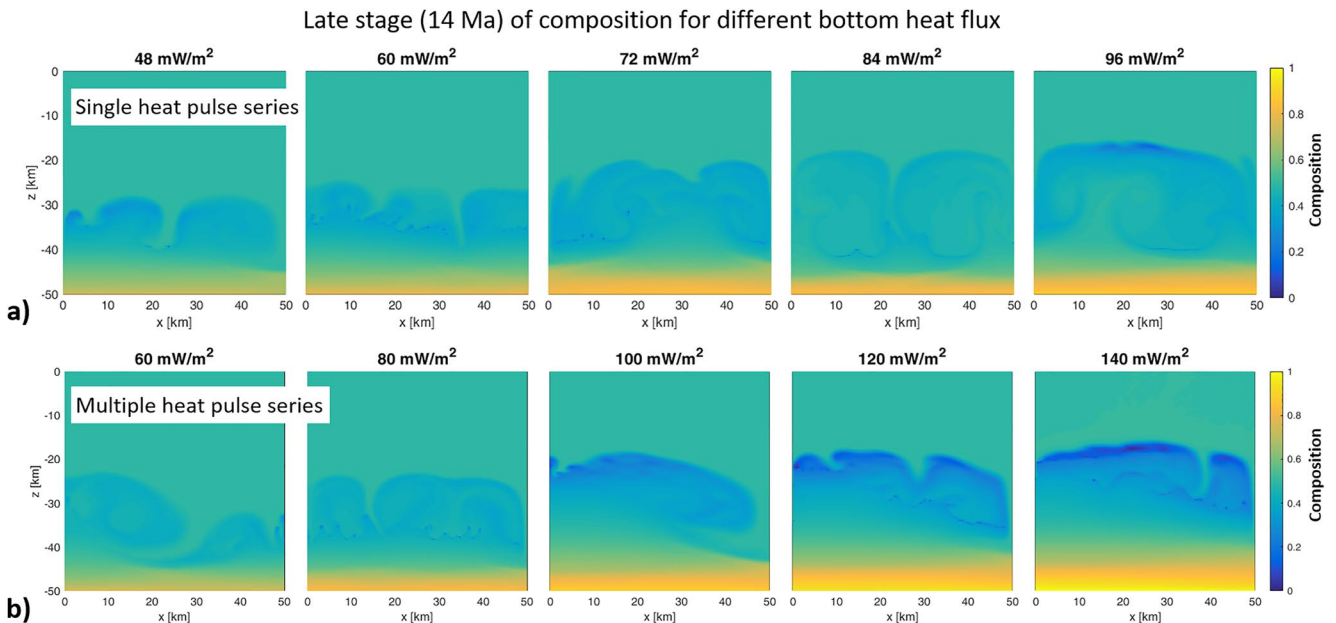


Figure 11. Composition at a late stage (14 Ma) for different bottom heat fluxes. (a) Models with a single heat pulse of 10 Ma duration with heat fluxes indicated by the subplot titles. (b) Models with multiple heat pulse of 2 Ma duration each with values indicated in the subplot titles. The time-integrated total heat input in the two models in each vertical column is equal.

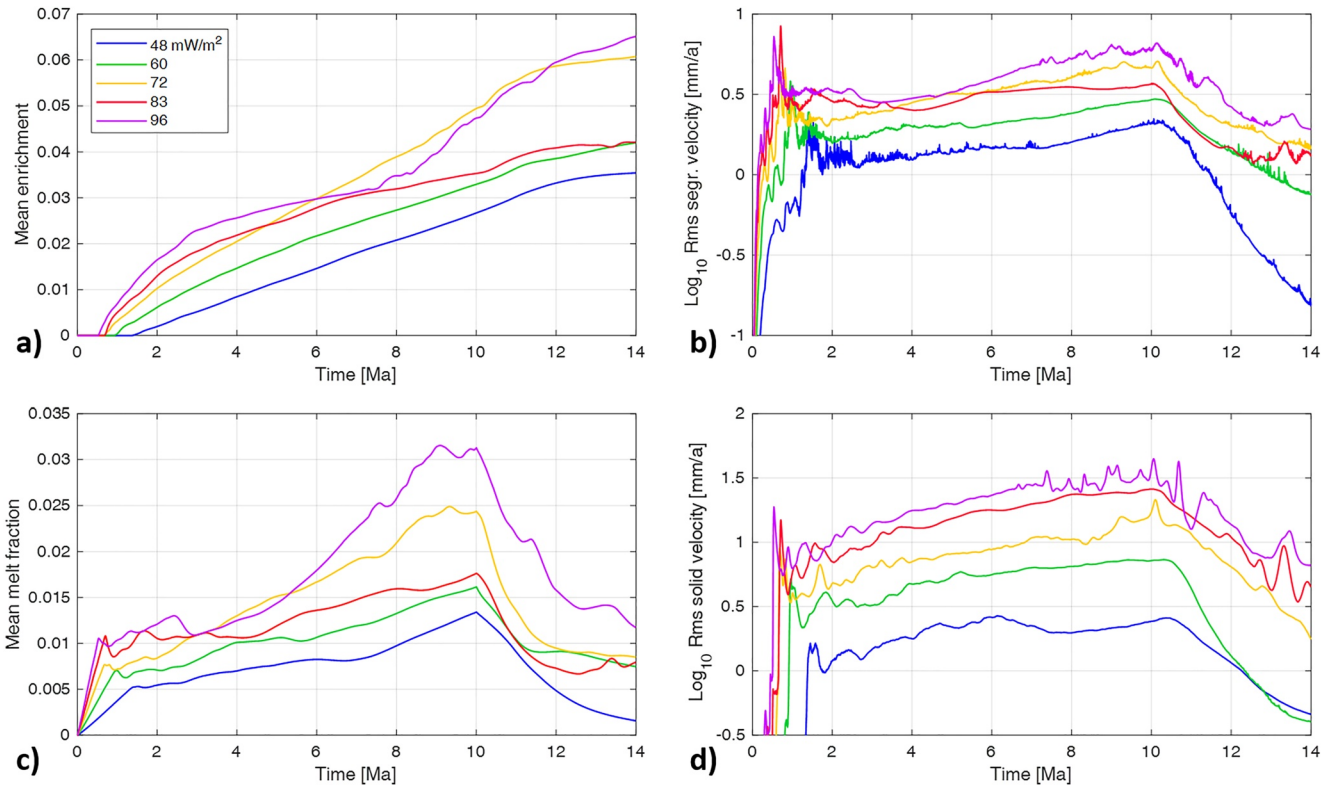


Figure 12. Effect of bottom heat flux pulse amplitudes (48, 60, 72, 84, and 96 mW/m²) for a single bottom heat flux pulse of 10 Ma duration. Temporal evolution of (a) mean enrichment, (b) root mean square (RMS) segregation velocity, (c) mean melt fraction, and (d) RMS solid velocity.

Increasing the heat flux from 60 to 84 mW/m² (for the single pulse heating case) intensifies convection and recycling. RMS velocities of the solid increase from about 6 to 25 mm/a, segregation velocities from 2 to ~5 mm/a (Figure 12). As will be discussed below, such ratios of segregation to solid velocities of less than 30% are indicative of the recycling mode, with multiple convective overturns, where solid velocities dominate with respect to melt velocities. During the late stage of the hottest model with 96 mW/m² (Figure 11a, right) RMS segregation velocities reach 6.3 mm/a (Figure 12b) (locally significantly higher) leading to some differentiation and emplacement of enriched material within the top of the partially molten layer near 15 km depth. Furthermore, the total amount of melt within the crust increases by about a factor three to a mean melt fraction of 0.03 (Figure 12c), equivalent to 75 km² of melt in 2D, or 3,750 km³ melt within an equivalent 50 × 50 × 50 km crustal volume in 3D.

In summary, for the single pulse heating case increasing the heat flux leads to a shallowing of the top of the partially molten zone from 30 to 15 km depth (Figure 13). Due to lower temperatures and high viscosity of the upper crust, the depth range between ~20 and 15 km is a strong boundary for magmas rising by convection and segregation. This implies that this is an accumulation zone for strongly evolved, enriched melts, and that upward from here, other modes of melt or melt-mush transport are necessary.

Results for the multiple heat pulse series (Figure 11b) shows that already for the coolest model with three 60 mW/m² pulses, equivalent to one 48 mW/m² single pulse, results in significantly shallower rise of the magmatic system, to about 23 km compared to 30 km. During each pulse the RMS velocities of the solid are about a factor 3 higher than in the single pulse model, forcing some recycling of enriched material compared to the weak single pulse model. Increasing the strength of the pulses to 100 mW/m² and above clearly shows that emplacement of enriched material is intensified with an extensive batholith between 15 and 25 km.

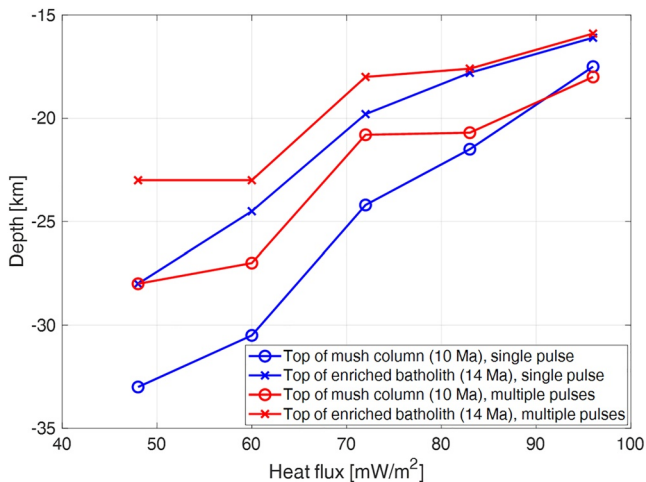


Figure 13. Depth of the top of mush columns and felsic batholith bodies as a function of heat flux. For the multiple pulse models the heat fluxes are equal to the time-integrated fluxes from 0 to 10 Ma of the single pulse models.

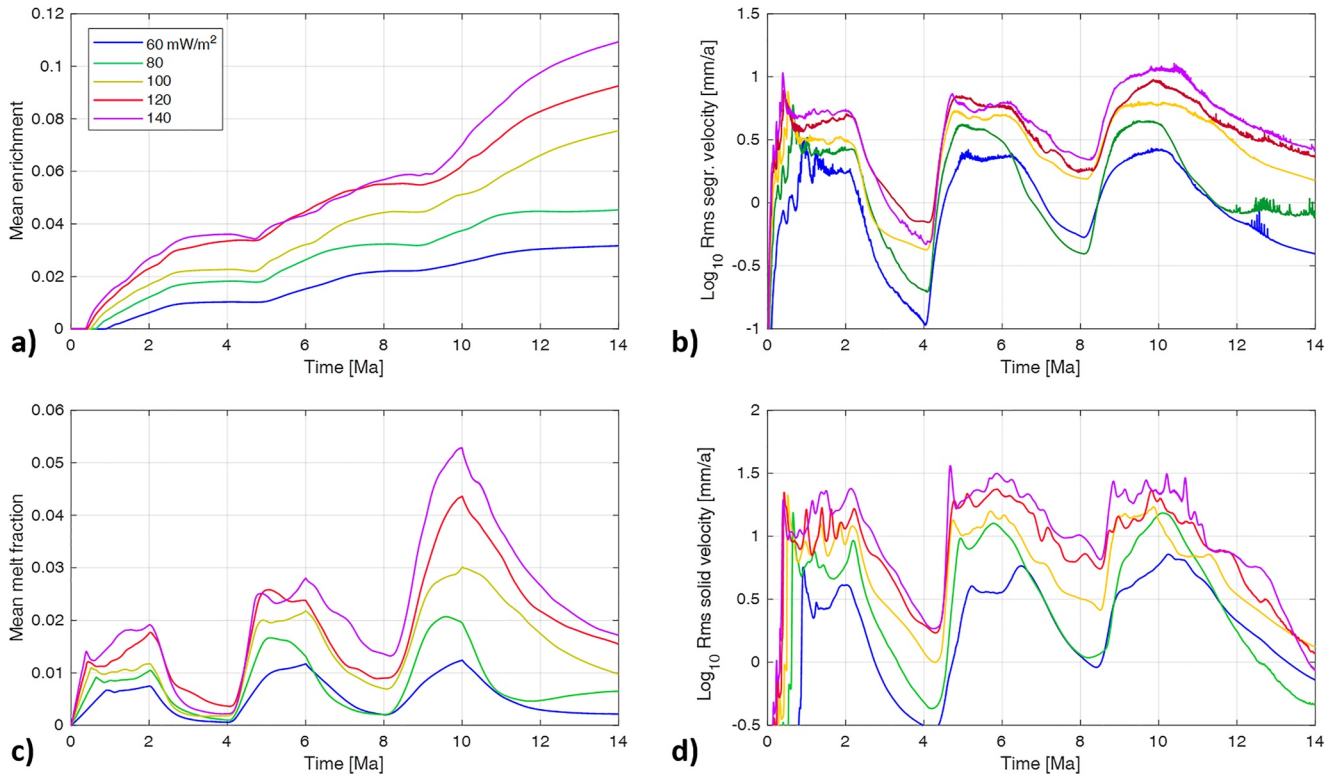


Figure 14. Effect of different heat pulse amplitude for the multiple heat pulse model with heat pulses lasting 2 Ma each. Temporal evolution of (a) mean enrichment, (b) root mean square (RMS) segregation velocity, (c) mean melt fraction, and (d) RMS solid velocity. The used heat pulses are indicated in the legend in panel (a). The time-integrated total heat input of the corresponding single and pulsed models are equal and represented by lines with the same color in Figure 12.

Comparing Figures 14b and 14d shows that the models with batholith emplacement rather than convective recycling are characterized by RMS segregation velocities reaching 11 mm/a or 30%–50% of the solid RMS velocities. Compared to the single pulse models the total amount of melt and enrichment are higher at 10 or 14 Ma, respectively (Figures 14a and 14c). The highest mean melt fraction of 0.05 is equivalent to 125 km² melt or 6,250 km³ in 3D in a 50 × 50 × 50 km section of the crust. A typical feature of the multiple pulse models with batholith emplacement is the heterogeneous spatial distribution of the batholiths (Figure 11b; 100, 120, and 140 mW/m²), sometimes three subsequent emplacement events are still visible as enrichment maxima at different depths.

Comparing the depths of the top of the partially melted mush columns and of the enriched batholith bodies (Figure 13) shows that for low to intermediate heat fluxes the multiple pulse models predict shallower depths. Thus, for the same time-integrated heat inputs, the pulsed models are more effective regarding melt ascent and batholith formation. By comparison, the melt and enriched material only ascend to similar depths of 16–17 km when the heat flux is highest in the single pulse case, but even in this case the batholith of enriched material is less voluminous (Figure 13).

3.4. Effect of Density of the Enriched Felsic Rock

In this section we study the effect of the density of the enriched solid material generated by melt solidification where the density of 100% enriched solid material corresponds to a density of felsic granite with 75% SiO₂ (Section 2.2). In the previous models, this density was 2,600 kg/m³ compared to the reference density of fertile rock of 2,700 kg/m³, the density of melt of 2,300 kg/m³ and the density of the residual, depleted rock of 3,100 kg/m³. Remember, that the thermal expansivity of all solid compositions and the melt is equal. Note that per definition the enrichment and depletion densities are for 100% enrichment and depletion, respectively. As discussed in Section 2.2, zero to 100% enrichment correspond to a solid composition of c_s varying from 0.5 to zero, while zero to 100% depletion correspond to c_s varying from 0.5 to 1. For further details about the effective densities used in the calculations see Schmeling et al. (2019).

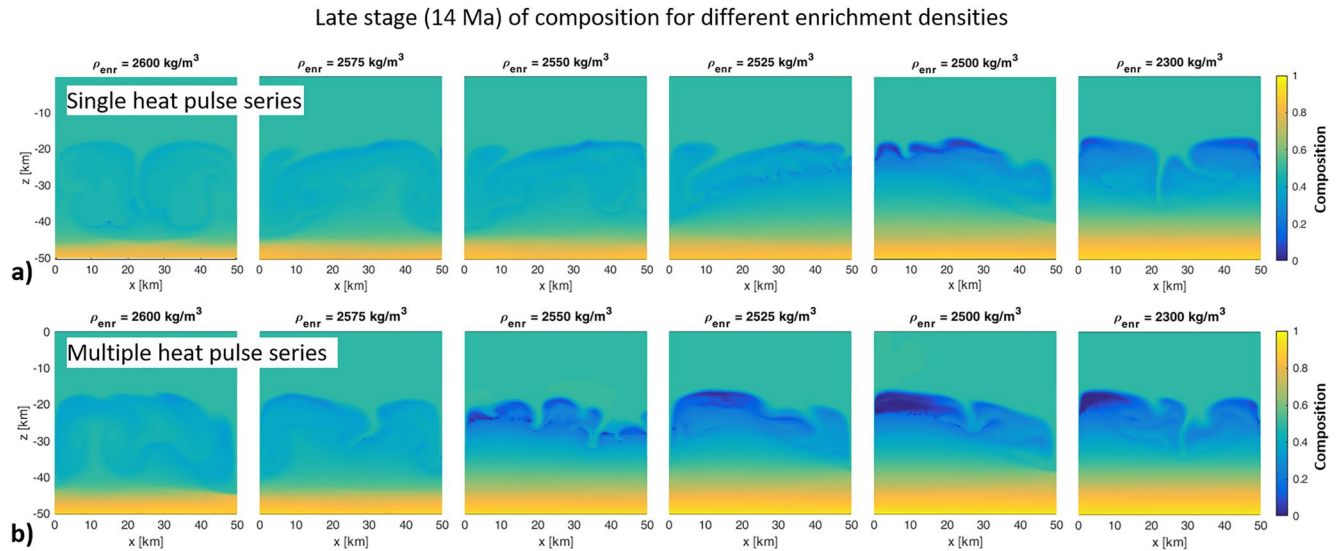


Figure 15. Late stage (14 Ma) of composition for different enrichment densities of the enriched solid material given above each figure. Previous models used $2,600 \text{ kg/m}^3$, the crustal reference density is $2,700 \text{ kg/m}^3$, and the melt density is $2,300 \text{ kg/m}^3$. In row (a) one 10 Ma long heat pulse of 84 mW/m^2 has been imposed. In row (b) three 2 Ma long single heat pulses of 140, 120, and 100 mW/m^2 have been imposed with the same total equivalent heat as in panel (a). The background bottom heat flux was 29.5 mW/m^2 .

The density of the enriched solid material is varied between $2,600$ and $2,300 \text{ kg/m}^3$ keeping the melt density at $2,300 \text{ kg/m}^3$. The solid value of $2,300 \text{ kg/m}^3$ is too low for igneous felsic rocks such as granites, which generally vary between $2,500$ and $2,800 \text{ kg/m}^3$, only rhyolites are lighter, with densities between $2,300$ and $2,500 \text{ kg/m}^3$ (e.g., Schön, 2015). The very low values used are meant for testing the sensitivity of the magmatic systems to the density of the enriched solid material.

Figure 15 shows the late stages of models with single and multiple heat pulses. A clear bifurcation exists between models with convective recycling of enriched material and models with batholith emplacement. This bifurcation takes place when the density of the enriched solid material becomes $<2,525 \text{ kg/m}^3$ for the single or $<2,575 \text{ kg/m}^3$ for the multiple pulse models. Once the density of the enriched solid material is below these values, batholith emplacement occurs and their overall appearance does not vary significantly anymore. Following the discussion in Sections 2.1 and 2.2, the Boussinesq approximation underestimates the volumes of enriched batholiths for the extremely low density values of the enriched material, such as $2,300 \text{ kg/m}^3$: the dark blue batholiths in the right-most models in Figure 15 may thus be about 10% smaller than without this approximation.

In Appendix D, we detail the effects of different densities of enriched rocks in mean enrichment, mean melt fraction, RMS segregation and solid velocities. These models can be used to elucidate the physics responsible for convective recycling and batholith emplacement, respectively. We discuss this in detail in Appendix D. The patterns observed indicate that in the recycling case, the segregation and solid velocities are relatively similar and the melt does not have time to segregate significantly from the solid matrix before freezing at the top of the convection cell, and is recycled back down where it melts preferentially because of its enriched nature. In contrast, for the batholith emplacement cases, the segregation velocities are about twice that of solid velocities. In this case, melt segregates forming a buoyant solid batholith that is displaced horizontally at emplacement level and only small volumes get recycled.

In conclusion, batholith emplacement is favored if the segregation velocity is significantly higher than the solid flow velocity, and convective recycling is favored if segregation is slow so that buoyant enriched material can be entrained into the downwelling flow to be remelted in the lower part.

3.5. Parameter Space for Batholith Emplacement Versus Convective Recycling

We have run 116 models with different retention numbers R_t , bottom heat fluxes (i.e., thermal Rayleigh numbers Ra_q , c.f. Equation 4), and enriched densities (i.e., enrichment Rayleigh numbers Ra_{enr} , c.f. Equation 4) both for multiple and single bottom heat pulses, including some cases with multiple pulses either decreasing or increasing with time (Figure 7). All models have been evaluated on whether they lead to batholith emplacement bodies after

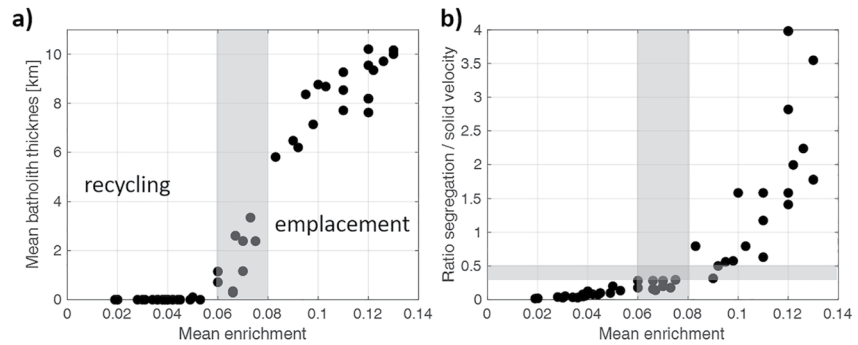


Figure 16. (a) Mean batholith thickness h_{bath} vs. mean enrichment at 14 Ma, (b) ratio of the root mean square (RMS) segregation velocity to the RMS solid velocity versus mean enrichment at ~ 10 Ma. All models have the same total bottom heating (either three pulses or one single pulse with an equivalent heat flux of 84 mW/m^2). The gray bands indicate the transitional ranges between emplacement and recycling.

14 Ma or convective recycling of enriched material. By calculating the area in which enrichment is larger than the lower bound defining granites (local enrichment of 0.314 corresponding to 63% SiO_2 , see Section 2.2) and normalizing this size by the width of the model (50 km), we obtain the mean thickness h_{bath} of the batholiths (Equation 8). Figure 16a shows the mean batholith thicknesses of all models with the same total bottom heat flux (single and multiple pulses) but different enrichment densities and retention numbers as a function of mean enrichment at 14 Ma. Up to a mean enrichment of about 0.06 no batholith emplacement occurs (i.e., local enrichment lies below 0.314 everywhere). Any SiO_2 rich material is recycled back into the lower crust. Within a narrow enrichment range of 0.06–0.08, finite batholith thicknesses develop (gray transition range) and rapidly increase up to 10 km. Thus, we can use the mean enrichment as a proxy for distinguishing between batholith emplacement or convective recycling modes. The ratio of the RMS of segregation velocity and solid flow velocity at ~ 10 Ma versus mean enrichment (Figure 16b) confirms that effective batholith emplacement correlates with RMS segregation velocities larger than 0.3–0.5 times the RMS solid velocity. This relation has been verified in detail for one example (Appendix D, Figure D3). It should be noted that taking the average or RMS of a quantity such as enrichment or velocity, respectively, depends on the model geometry, particularly on the size of the regions with a non-zero quantity with respect to the total model domain including the unmolten and stagnant regions. Therefore, the actual values discussed above may not be easily generalized, but allow consistent and meaningful comparisons among the models. As a rule of thumb, inspection of the models indicates that in all cases where the RMS segregation to solid velocity ratios exceed 0.3–0.5, locally the segregation velocity exceeds the solid velocity by a factor 3 or more, especially in regions of small solid velocity. Such high segregation velocities effectively reinforce the formation of batholiths.

In Figure 17 we explore the parameter spaces $Ra_{\text{enr}} - Rt$ and $Ra_{\text{enr}} - Ra_q$ by plotting the mean batholith thicknesses after 14 Ma of all models as functions of Ra_{enr} , Rt , and Ra_q . Low Rt means high mobility of the melt, and high Ra_{enr} means low density of enriched solid material with respect to fertile crust, so that segregation is enhanced in models with low Rt and high Ra_{enr} . The yellow dots indicate models without batholiths, that is, where the enriched material has been recycled back into the lower crust by thermal and phase-change-driven convection. The blue dots indicate models in which significant batholiths with thicknesses of several km have developed. In all model sets, a relatively sharp boundary exists (approximated by dashed curves) separating the recycling domain from the batholith emplacement domain. In the $Ra_{\text{enr}} - Rt$ parameter space, high melt mobility (low Rt) and lower density of enriched solid material (higher Ra_{enr}) favor emplacement while lower melt mobility and higher enrichment densities favor recycling. Comparing multiple equal pulse models to models with three pulses of decreasing amplitude with time and with a single pulse clearly shows different behaviors (Figures 17a–17c). Three equal pulses (Figure 17a) shift the boundary between the regimes to higher Rt , that is, lead to a more pronounced emplacement behavior compared to the others. This may be explained as follows: switching off the bottom heat pulse several times hampers recycling because convection slows down after each pulse while segregation still takes place during the intervals of paused heat flux.

We now fix the melt mobility to $Rt = 3$, which is near the boundary between recycling and batholith emplacement in Figures 17a–17c, and explore the parameter space $Ra_{\text{enr}} - Ra_q$. Increasing the convective vigor by increasing the bottom heat flux (i.e., increasing Ra_q) favors batholith emplacement (blue dots in Figures 17d–17e). We

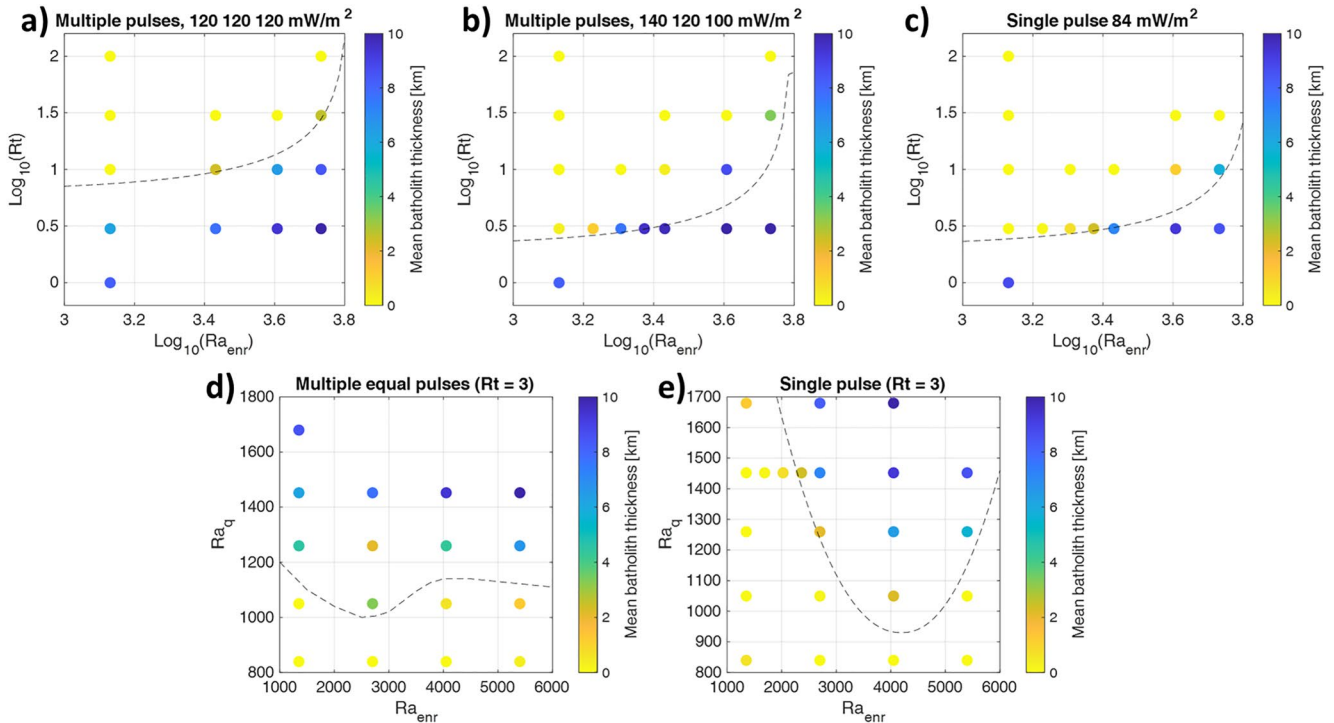


Figure 17. Diagrams distinguishing the batholith emplacement (orange to blue dots) versus convective (no batholiths, yellow dots) regimes in the $\text{Ra}_{\text{enr}} - \text{Rt}$ and $\text{Ra}_{\text{enr}} - \text{Ra}_q$ spaces. Models in panels (a–c) had an integrated total bottom heat flux corresponding to the heat flux Rayleigh number $\text{Ra}_q = 1470$. The models in panels (d, e) have a retention number $\text{Rt} = 3$. (a) Three equal heat pulses of 120 mW/m^2 with 2 Ma duration, (b) three heat pulses of 140, 120, and 100 mW/m^2 , and (c) single 10 Ma long heat pulse of 84 mW/m^2 . In (a–c) the total time-integrated heat input was identical over 10 Ma and the dashed curves show the boundaries between batholith emplacement and granite recycling cases calculated by the scaling law (Section 3.6). Fits were obtained with the parameters: (a) $\varphi = 0.09$; $f = 0.15$; $a_0 = 0.5$, (b) $\varphi = 0.05$; $f = 0.14$; $a_0 = 0.5$, and (c) $\varphi = 0.05$; $f = 0.13$; $a_0 = 0.5$. (d) Three equal heat pulses with magnitudes varied from 60 to 140 mW/m^2 corresponding to Ra_q from 840 to 1,680. (e) Single 10 Ma long heat pulses varied from 48 to 96 mW/m^2 , corresponding to the same Ra_q values as in panel (d). The dashed lines show the boundaries between the emplacement and recycled models estimated by visual inspection.

explain this by the strong increase in total melt fraction which segregates due to the chosen mobility and stays buoyant after solidification. Only for small Ra_{enr} this buoyancy is not sufficient for batholith emplacement and the felsic material is recycled (Figure 17e). The slight preference for recycling also at high Ra_{enr} (e.g., 6,000) as suggested by Figure 17e needs an explanation. Evaluating the models within the lower right of Figure 17e in detail (not shown) suggests that segregation velocities within the slow rising plumes (because of low heat flow) are reduced due to freezing already within these plumes. Due to freezing, the solid within the plumes becomes enriched, increasing the total buoyancy within the plumes and thus increasing the convective vigor. However, the melt is less buoyant or even denser with respect to the buoyant enriched matrix, which decreases segregation. As a result, convection and associated recycling is enhanced at very low enrichment densities of $2,300 \text{ kg/m}^3$ ($\text{Ra}_{\text{enr}} > 5,000$) at small Ra_q . Comparing the models with three pulses and a single pulse for low enrichment buoyancy (low Ra_{enr}) supports the previous observation of favoring batholith formation when multiple pulses are involved instead of a single one (Figures 17d and 17e).

3.6. An Analytical Scaling Law for Batholith Emplacement Versus Convective Recycling

From the evaluations of the parameter space in Section 3.5, a clear boundary emerges between cases with batholith emplacement and cases of convective recycling. In Appendix C, we derive an analytical scaling law for such a boundary by defining a batholith emplacement parameter, e_b . The emplacement of enriched silicic material takes place predominantly within the upper horizontal limb of the convective flow by segregation. Relating the characteristic segregation time t_{sgr} of the melt to leave the horizontal convection limb to the characteristic time t_{hor} of a solid particle to travel along the horizontal limb, we define the emplacement parameter as:

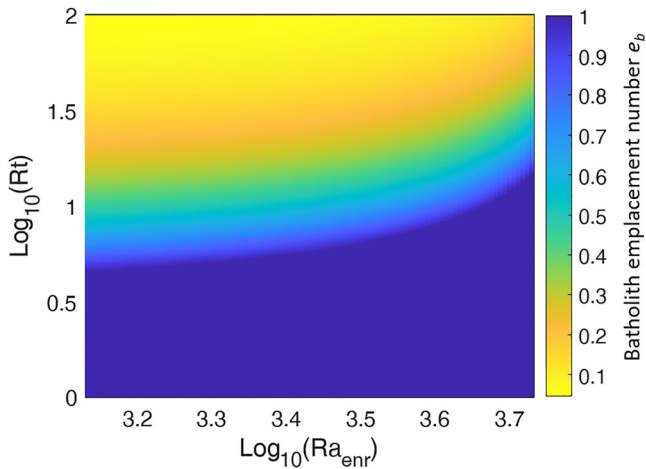


Figure 18. Regime diagram for the analytical batholith emplacement number e_b (Equation 11 truncated at 1) in the parameter space $Rt - Ra_{\text{enr}}$. Batholith emplacement is favored by low Rt and high Ra_{enr} , because they increase segregation and buoyancy. Used values are $\varphi = 0.1$, $f = 0.15$, $a_0 = 0.5$. Other assumptions: $Ra_f = 1470$, $Ra_m = 5400$.

$$e_b \equiv \begin{cases} \frac{t_{\text{hor}}}{t_{\text{sgr}}} & \text{if } t_{\text{sgr}} \geq t_{\text{hor}} \\ 1 & \text{if } t_{\text{sgr}} < t_{\text{hor}} \end{cases} \quad (10)$$

If $t_{\text{sgr}} \geq t_{\text{hor}}$ only a fraction of the available melt contributes to emplacement, and this fraction scales with the ratio of these times, that is, e_b . If $t_{\text{sgr}} < t_{\text{hor}}$ melt has enough time to fully segregate out of the partially molten horizontally flowing layer to form a batholith, and we truncate e_b at 1 to define the case of batholith emplacement. Estimating these characteristic times using Darcy's law and convective scaling laws including effective Rayleigh numbers, we arrive at (for details, see Appendix C):

$$e_b = \frac{Ra_f}{Rt} \frac{\varphi^{n_\varphi - 1}}{ba_0 \left(1 - \frac{eRa_{\text{enr}}}{Ra_{\text{eff}}}\right) Ra_{\text{eff}}^\gamma} \quad (11)$$

truncated at 1. The important unknown parameters controlling e_b are the average melt fraction φ in the partially molten regions, the typical degree of enrichment e , and the non-dimensional thickness of the upper layer a_0 in which horizontal flow occurs and segregation takes place (see Appendix C). Inspecting several models complemented by some tests shows that reasonable guesses may be: $\varphi = 0.1$, $e = 0.15$, $a_0 = 0.5$. Figure 18 shows e_b as a

function of Ra_{enr} and Rt in a similar range as the observed mean batholith thicknesses from the numerical models. A good general agreement is found when compared to the empirical results shown in Figures 17a–17c. A similar derivation of a scaling law for emplacement or recycling for constant Rt but various bottom heat fluxes, Ra_q , as shown in the regime diagrams Figures 17d and 17e does not work because for small Rayleigh numbers the scaling law for the convection velocity breaks down, as the Rayleigh numbers are close to the critical Rayleigh number.

The regime boundaries in Figures 17a–17c can be defined by parameter combinations Rt and Ra_{enr} at which the emplacement parameter e_b is equal to $e_{b05} = 0.5$. Inserting this value into Equation 11 gives the boundary retention number $Rt_b = Rt(Ra_{\text{enr}}, e_b = e_{b05})$. We can rewrite this equation in dimensional form by solving for the least known parameters: melt viscosity η_f as a function of mean distances between pores or channels, d

$$\eta_f|_{\text{boun}} = \frac{\Delta\rho_f g h d^2 \varphi^{n_\varphi - 1}}{\kappa C e_{b05} b a_0 \left(1 - \frac{\Delta\rho_{\text{enr}} e}{\frac{\rho_0 a q h}{\lambda} + \Delta\rho_f \varphi - \Delta\rho_{\text{enr}} e}\right) Ra_{\text{eff}}^\gamma} \quad (12)$$

All terms are defined in Table 1 or Appendix C. Assuming typical values for $\Delta\rho_{\text{enr}} = 100$ up to 400 kg/m^3 , Equation 12 is plotted in Figure 19 as a function of grain size or distance d between melt channels. The resulting lines divide the viscosity- d space into the regimes “batholith emplacement” and “convective recycling.” While for melt flow on grain scale, low viscosities of 10^5 Pa s or smaller are needed to generate granitic batholiths, melt channels with distances of meters to 10 m (Symington et al., 2014) allow formation of batholiths for viscosities of $<10^{10} \text{ Pa s}$. The latter viscosities are in the range of dry granite melts, while the smaller ones require wet melts. Increasing the total heat input, Ra_q , accelerates both thermal and phase-change-driven convection as well as melt segregation. This favors batholith emplacement and shifts the boundary upwards to higher melt viscosities (Figure 19, dot-dashed curve).

4. Discussion

4.1. Limitations and Assumptions

One severe simplifying assumption in the models is the constant viscosity of the melt, while for the solid we used a more realistic visco-plastic rheology. Melt viscosity depends on temperature, SiO_2 content and water. Melts generated from fertile rocks during the early evolution of our models are expected to be more water-rich and less evolved. Both effects result in low melt viscosities, which will increase by perhaps three orders of magnitude as the melts become less water-rich and more evolved during further evolution of the model. At later stages, the depletion of source rock increases and probably its water content decreases, thus, the melt temperature is higher due to a higher solidus

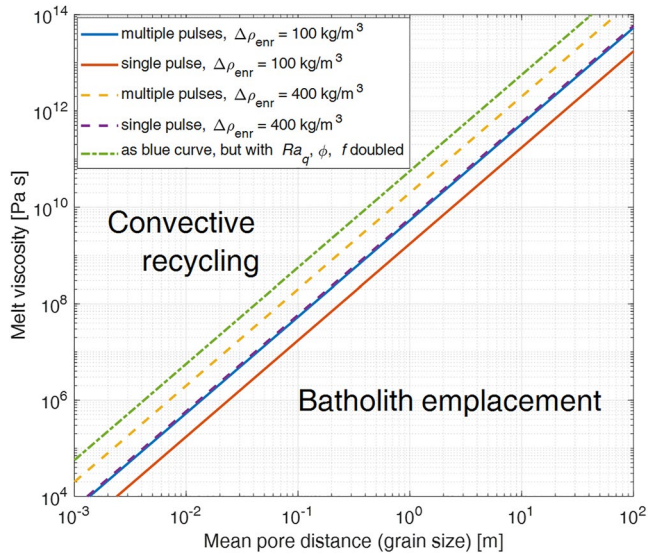


Figure 19. The boundaries between the “batholith emplacement” and the “convective recycling” regimes of Figures 17a and 17c are plotted in a dimensional diagram of melt viscosity versus mean pore distance (or grain size). Further assumptions are $h = 50$ km, $\kappa = 0.9259 \cdot 10^{-6} \text{ m}^2 \text{ s}^{-1}$, $\eta_0 = 10^{20} \text{ Pa s}$, $C = 100$, $n_\phi = 3$, $b = 0.354$, $\gamma = 0.5$, $\alpha = 2.4 \cdot 10^{-5} \text{ K}^{-1}$, $\rho_0 = 2700 \text{ kg m}^{-3}$, $\Delta\rho_f = 400 \text{ kg m}^{-3}$. For each curve Rt is constant with values between 4.3 and 141. Solid and dashed curves are based on an integrated total heat flux of 84 mW/m^2 during a single heat pulse time of 10 Ma. For the green dot-dashed curve the heat input (i.e., Ra_q) was doubled, as well as the average melt fraction ϕ and enrichment f .

temperature of the depleted rock. A higher temperature is expected to reduce the viscosity by perhaps one order of magnitude. Thus, in total we expect that as enrichment increases in the active parts of the models the melts become stiffer as they evolve. The melt viscosity has only a minor effect on the dynamics of the mush (partially molten mixture) as long as the melt fraction is below the disaggregation limit $\sim 20\% \sim 50\%$ and the two-phase flow is in the low viscosity regime ($\eta_f \ll \eta_s$). However, melt viscosity strongly controls the segregation velocity. Thus, during early stages the magmatic system may be characterized by lower retention numbers than during later stages. A time-dependent variation of the effective retention number is a future goal and might also have some effect on the heterogeneity or stratification of the evolving batholiths.

As discussed in Schmeling et al. (2019), once the porosity reaches or exceeds the disaggregation limit, we use a numerical truncation value for melt viscosity, which mimics highly viscous dry silicic melts. This is a severe assumption, which neglects short-term flow processes within the evolving magma chambers. Another important neglected factor is the possibility that melt may ascend as dykes and magma conduits. This limits the applicability of our models to depths >15 km. First tests with models in which melt exceeding some critical melt fraction is extracted and transferred to shallower depth are promising.

To our knowledge, all dynamical modeling approaches of magmatic systems assume isotropic distributions of melts. However, there are indications from magnetotellurics that in the mush zone the melt may be distributed anisotropically (e.g., beneath the Ceboruco Volcano (Mexico) at mid- to lower-crustal depths (Hering et al., 2022)). Coupling flow stresses in a mush with the orientation of melt inclusions to formulate an anisotropic permeability tensor and including it into the Darcy equations is a challenging topic, which should be addressed in the future.

Our initial condition assumes an unmolten crust close to the solidus temperature at the bottom of the model and mimics basaltic underplating by a thermal boundary condition. Another endmember would be an already strongly molten lower crust. This has been studied in detail by Schmeling et al. (2019). Another possible initial condition could model the crustal intraplating of basaltic magma as in Annen et al. (2015). However, this would require distinguishing between two types of melts using two melting curves and compositionally extending our model to three or four components.

For all models in this study, single or multiple heat pulses at the bottom have been assumed to mimic magmatic underplating events. An alternative condition would be prescribing an increased bottom temperature during such pulses. Tests show several differences in the evolution: in case of sudden temperature increase, strong plumes (or diapirs) with melt caps develop, while for increased bottom heat flux, melting is weaker and more spatially distributed. However, for the second and third heating events in the case of prescribed heat flow, more fertile material is still present at depth and leads to more wide-spread melting for these later pulses. Another difference is that the mean melt fraction is much higher for the first heat pulse in the prescribed bottom temperature case and decreases to almost zero during the cooling intervals. For the bottom heat flux case, more melt is still present during the cooling intervals and melt segregation is continuous leading to enriched silicic material being emplaced at shallower depths.

The heat flow boundary condition also allows a better control of the total heat energy input because the switching off of the temperature pulse temporarily causes a downward heat loss from the crust to the mantle. Thus, the constant temperature boundary condition is unrealistic. In fact, a compromise between these two end-member boundary conditions would be a Robin boundary condition in which a superposition of bottom temperature and heat flux are prescribed. This could be formulated to mimic an initially hot conductive layer of finite thickness below our model whose bottom temperature is fixed.

4.2. Effect of Pulse Duration and Number of Pulses

Our reference models with a single and with three 2 Ma heat pulses resulted in each of the two modes of convective recycling and batholith emplacement, respectively. It is interesting to test the effect of more than three pulses, that is, $N > 3$, and the role of the ratio of pulse duration to the intervals in between, defined as a . Keeping the total heat input and the total time window of 10 Ma, we ran a few extra models with $N = 5$, $a = 1$ and with $N = 3$ and a varying between 0.22 and 2. Variation of a strongly influences the extra heat flux of each of the pulses, while for higher frequency the heat input variations are dampened. Evaluating the models with respect to the two modes of batholith emplacement and convective recycling shows that shorter but more intense pulses ($a < 1$) favor segregation and thus batholith formation, while longer ($a > 1$, corresponding to shorter gaps between the pulses) or higher frequency pulses ($N > 3$) favor convective recycling.

4.3. Comparison to Magmatic Systems in Continental Crust: Altiplano-Puna and Tibetan Plateaus

The models were inspired by the Altiplano-Puna Plateau but the results have implications also to the Tibetan Plateau and other thickened crusts. In this section, we explore these implications keeping in mind the limitations of our models. In both cases, the low-velocity seismic zones define the presence of melt at depths >15 km (del Potro et al., 2013; Fialko & Pearce, 2012; Gottsmann et al., 2017; Nelson et al., 1996; Unsworth et al., 2005). We argue that Altiplano-Puna Plateau and the Tibetan Plateau may represent the two modes of behavior—the batholith emplacement and the convection recycling, respectively.

4.3.1. Altiplano-Puna Plateau: Batholith Emplacement Mode

The batholith emplacement mode is characterized by mush zones with melt-rich caps that could feed intense volcanism. We argue that the Altiplano-Puna Plateau could be an example of this mode with intense volcanism in the last 10 Ma (de Silva & Gosnold, 2007; de Silva et al., 2015; Folkes et al., 2011), including a large region being currently uplifted, pushed by magmas underneath, centered around the Uturuncu volcano (Fialko & Pearce, 2012; del Potro et al., 2013).

After 10 Ma our models reach temperatures at 20–25 km depth well in agreement with the reference temperature suggested for the Plateau by Gottsmann et al. (2017). Their higher temperatures for the shallower plumbing system are not modeled here. It is interesting to compare the melt segregation flux of our models with the current andesitic melt flux of $\sim 2 \cdot 10^7$ m³/a modeled beneath the Uturuncu volcano based on uplift and subsidence rates (Gottsmann et al., 2017). The averaged (RMS) segregation velocities of our reference models at 10 Ma model time in Section 3.1 are ~ 3 or 10 mm/a for continuous or pulsed heating events (Figure 4b), respectively. These values have to be multiplied by a factor of ~ 2 if averaging would include only the lower half of the model, namely the partially molten source zone. Multiplying the resulting average segregation velocity by a representative area of 50×50 km we arrive at a melt segregation flux of $1.5 \cdot 10^7$ or $5 \cdot 10^7$ m³/a for the single or multiple pulse models, respectively. These values are in good agreement with Gottsmann et al. (2017) values indicating that their estimate could also be representative of the long-term segregation rates and not only the current melt segregation flux.

While the depth of the minimum low-shear-velocity anomaly beneath the APVC is between 10 and 20 km depth (Ward et al., 2014), our models give the depth of the top of the melt zones between 18 and 33 km for the various heat inputs (c.f. Figure 13). Shallower depths are expected for (a) an increased bottom heat flux during the pulses, (b) a weaker crustal rheology, or (c) additional melt ascent out of the melt-rich caps by dykes, which is not accounted for here. As for (a), an extrapolation of the depths of the top of the molten zones (Figure 13) to 10 km depth requires 116 mW/m² for a single 10 Ma pulse or 190 mW/m² for three 2 Ma pulses. As for (b), choosing other published wet granite or quartz rheologies would shift these depths by 4 km at most.

Van Zalinge et al. (2022) used geochronology data of the Oxayan Formation (Central Andes) to constrain the minimum duration of pluton growth of 4.6 Ma and subsequent ignimbritic eruptions. They used Rayleigh-Taylor instability characteristics and a simple conduit flow model to arrive at a reasonable transport model of a middle crustal mush zone feeding a shallower magma chamber. They used 10^5 Pa s for the silicic melt viscosity and a conduit width of order 5 m corresponding to large conduit distances. From Figure 19, such parameters lie well within the “batholith emplacement” regime.

4.3.2. Tibetan Plateau and Others: Recycling Mode

Unlike the Altiplano-Puna Plateau, magmatism in Tibet for the last 10 Ma is minor and typically concentrated to central and northern Tibet (Guo & Wilson, 2019; Wang et al., 2016). Our convective recycling mode requires anomalous high mantle heating and subsequently high surface heat flux (e.g., Figure 6a) but does not lead to significant accumulation of eruptible melt at the top of the rising plumes. This is because melt extraction is inefficient because of high melt viscosity (requiring highly silicic dry melts, c.f. Figure 19), high melt density or small melt fractions, or relatively rapid phase-change-driven convective overturns. In this mode, surface volcanism is expected to be weak or absent, explaining the absence of widespread volcanism in Tibet despite the widespread presence of shallow magmatic mushes. Another possible candidate for this mode of behavior is the low-seismic velocity zone beneath central Taiwan which has been interpreted as partial melting but which is unrelated to volcanism (Ma et al., 1996).

5. Conclusion

Dynamic models of magmatic systems in continental crust heated from below show a diversity of magmatic scenarios depending on the temporal heating modes, melt mobility, and density of evolved melts and residual rocks. The heating modes have been designed to represent basaltic underplating events on time scales of up to 10 Ma. In all models, melting occurs in the lower crust and melt segregates and rises by a combination of porous flow and diapiric flow of the partially molten mass. This mass represents the rising mushy limb of lower crustal convection cells driven by the heat input and phase change related to melting, melt segregation and solidification of an enriched rock extracted from a residual rock. The maximum ascent height of the evolving mush columns, with or without melt-rich caps, depends on the total heat input and ranges from 33 to 18 km depth. Above these depths, crustal viscosity becomes too high to allow for significant rise by viscous flow and further ascent of magma requires dykes or volcanic conduits not included in the models.

We compared the behavior of two temporal heating modes: (a) the single heating event lasting 10 Ma and (b) the three 2 Ma long pulses of anomalous bottom heat flux, distributed over a total time of 10 Ma. Despite them having the same integrated extra heat input, the total amount of magma and enriched, silicic rocks generated for the pulsed model was larger and the resulting batholiths were more heterogeneously distributed in space.

Two main modes of model behavior have been found:

1. Batholith emplacement mode, where silicic melts segregate from the rising and horizontally flowing upper part of the convection mush zones and form large bodies of evolved granitic rocks. In the lower crust a thick layer of depleted, restitic rock forms.
2. Convective recycling mode, where silicic melts do not segregate and accumulate to form batholiths. Instead, melt solidifies within the mush and is recycled back into the lower crust by the downwelling limbs of the convection cells where it undergoes remelting. Only thin depleted restitic layers form in this case.

Which of these two classes is favored depends on several factors: mode (a) is favored by relatively high total amplitude of the heat input and multiple versus single heat pulses, high melt mobility (low melt viscosity, high rock permeability), and relatively low density of the melt and the evolved, silicic rock. Mode (b) is favored by the less intense, but not too small heat input, less mobile melt and denser melts or evolved rocks. The distinction between the two modes can be formulated by a non-dimensional scaling law and depends on the thermal, melt and compositional Rayleigh number and the retention number, which controls melt mobility. The magmatic system of the Altiplano-Puna Plateau is a possible example of mode (a) “batholith emplacement,” while the Tibetan Plateau and Central Taiwan are possible examples of mode (b) “convective recycling.”

Appendix A: The Governing Equations

In this Appendix the governing equations of our two-phase flow approach are listed. They are taken from Schmeling et al. (2019) where more detailed discussion can be found. For the definition of quantities see Table 1.

The equations of conservation of mass, momentum, and energy are given as

$$\rho_f \left(\frac{\partial \varphi}{\partial t} + \bar{\nabla} \cdot (\varphi \bar{v}_f) \right) = \Gamma, \quad (\text{A1})$$

$$\rho_s \left(\frac{\partial(1-\varphi)}{\partial t} + \bar{\nabla} \cdot ((1-\varphi)\bar{v}_s) \right) = -\Gamma, \quad (\text{A2})$$

$$\bar{v}_f - \bar{v}_s = -\frac{k}{\eta_f \varphi} (\bar{\nabla} P - \rho_f \bar{g}), \quad (\text{A3})$$

$$\rho \bar{g} - \bar{\nabla} P + \frac{\partial \tau_{ij}}{\partial x_j} = 0, \quad (\text{A4})$$

$$\rho c_p \left(\frac{\partial T}{\partial t} + \bar{v} \cdot \bar{\nabla} T \right) = \bar{\nabla} \cdot (\lambda \bar{\nabla} T) + \rho H - L\Gamma, \quad (\text{A5})$$

with the viscous stress tensor and averaged flow velocity, respectively

$$\tau_{ij} = \eta_s \left(\frac{\partial v_{si}}{\partial x_j} + \frac{\partial v_{sj}}{\partial x_i} \right) + \left(\eta_b - \frac{2}{3} \eta_s \right) \delta_{ij} \bar{\nabla} \cdot \bar{v}_s, \quad (\text{A6})$$

$$\bar{v} = \varphi \cdot \bar{v}_f + (1-\varphi) \cdot \bar{v}_s. \quad (\text{A7})$$

The visco-plastic solid viscosity is given as

$$\frac{1}{\eta_s} = \frac{1}{\eta'_\varphi} \left(\frac{1}{\eta_{MC}} + \frac{1}{\eta_{duc}} \right) \quad (\text{A8})$$

$$\eta_{MC} = \frac{\tau_{max}}{2\dot{\epsilon}_{II}}, \eta_{duc} = A_{duc} \cdot \exp\left(\frac{E + V P_{Lith}}{RT_{abs}}\right) \cdot \dot{\epsilon}_{II}^{\frac{1}{n}-1}, \quad (\text{A9})$$

$$\tau_{max} = A \cdot \bar{z} + B \quad (\text{A10})$$

and the non-dimensional porosity-dependent parts of the shear and bulk viscosities in Equation A8 are defined as

$$\eta'_\varphi = \left(1 - \frac{\varphi}{c_1}\right)^{k_1}, \eta'_b = c_2 \frac{(c_1 - \varphi)^{k_2}}{\varphi} \text{ for } \varphi < c_1, \quad (\text{A11})$$

respectively. For values used in the approximation Equation A11 and the finite viscosity stabilization formulation used at porosities above the disaggregation porosity, $c_1 = 0.505$, see Schmeling et al. (2019).

The actual parameter values (Table 1) are taken from Table 2 of Schmeling et al. (2019), which contains a misprint: the activation volume should be $10^{-5} \text{ m}^3 \text{ Mol}^{-1}$. We note that even when taking a zero activation volume, the results in Schmeling et al. (2019) are almost identical to those that they obtained. Another misprint in Schmeling et al. (2019) concerns Equation 14 in that paper, which should be replaced by Equation A9.

Non-dimensionalizing the equations, eliminating the pressure by combining Equations A3 and A4 and replacing the solid velocities with the stream function and irrotational velocity potential, the equations are solved by the code FDCON (see Schmeling et al. (2019) and references therein) on a grid with resolution of 101×101 for the momentum equation of the solid phase, while 201×201 is assumed for the melt momentum and mass equations, the composition equations and the energy equation. The solid velocities and viscosities are taken as arithmetic, geometric or harmonic means at the sides or cell interiors to go into the FD-equations of the temperature and melt-transport equations.

Appendix B: The Melting Law

Numerically, melting is calculated in the following way: During one time step the solid and melt compositions are advected separately using an advection equation of the type

$$\frac{\partial c_{f,s}}{\partial t} + v_{f,s} \cdot \nabla c_{f,s} = 0, \quad (\text{B1})$$

where $v_{f,s}$ is the melt and solid velocity, respectively (Equation A11 in Schmeling et al. (2019)). During the same time step of segregating the melt, a new φ -field is calculated by solving the melt momentum equation, and after

advection on different paths the solid and melt compositions c_s, c_f as well as the temperature T are obtained. At this stage of calculation latent heat is not yet included in the temperature field. With these variables the mean composition at any point is given by Equation 7. From T and c the melting increment to reach an equilibrium melt fraction (Equation 6) is calculated by iteration. We start the iteration $i = 1$ at any position with the present melt fraction $\varphi_i = \varphi$ and temperature $T_i = T$ and determine φ_{equ_i} of the i th iteration by the lever rule

$$\varphi_{\text{equ}_i} = \frac{c - c_s(T_i)}{c_f(T_i) - c_s(T_i)}. \quad (\text{B2})$$

Note that c remains fixed during the iteration and $c_f(T_i), c_s(T_i)$ are the c_f and c_s —values on the liquidus and solidus curves, respectively, that is, they are different from the previously advected values. The melting increment needed to reach the equilibrium value would be $\delta\varphi_i = \varphi_{\text{equ}_i} - \varphi_i$ if no latent heat would be released or consumed. Thus, to account for this, we underrelax the increment by delay and get the melt fraction of the next iteration

$$\varphi_{i+1} = \varphi_i + \delta\varphi_i(1 - \text{delay}) = \varphi_i + \delta\varphi_i' \quad (\text{B3})$$

This increment $\delta\varphi_i'$ contributes cumulatively to the melt generation rate

$$\Gamma_{i+1} = \Gamma_i + \frac{\delta\varphi_i'}{dt}, \quad (\text{B4})$$

where the starting melt generation rate was set to $\Gamma_1 = 0$. The melting increment is also associated with a simultaneous local change of temperature. The temperature of the next iteration is

$$T_{i+1} = T_i - L\delta\varphi_i'. \quad (\text{B5})$$

With this new temperature a new equilibrium melt fraction can be determined by setting $i = i + 1$ and jumping to Equation B2. The iteration converges if the change in melt generation rate $\delta\varphi_i'/dt$ falls below a small threshold (or more precisely, the last n increments fall below a threshold). Note that the iteration does not change c , only c_f, c_s . Near the compositions $c = 0$ or $c = 1$ the T -dependence of melt fraction is very strong and requires a strong damping with delay > 0.9 . Thus, an automatic c —dependent delay is used with the formula

$$\text{delay} = (1 - [1 - (\cos(2\pi c) + 1)/2]^{\text{pow}}) \cdot (1 - \text{delay0}) + \text{delay0} \quad (\text{B6})$$

Good results are achieved with $\text{delay0} = 0.6$ and $\text{pow} = 2$. As delay can approach 1 very closely its maximum value is truncated at 0.995.

To mimic a binary eutectic system with compositions A and B the composition $c = 0$ is assumed to represent the eutectic composition and the composition $c = 1$ represents composition B. The solidus curve is assumed to be almost horizontal at the eutectic temperature with a numerically necessary non-zero slope and a sharp kink near $c = 1$ rising to the melting temperature of pure composition B. There it merges with the liquidus curve. Applying the lever rule as in the solid solution case above gives a sub-vertical melt fraction curve near the solidus temperature (due to the sub-horizontal solidus curve) followed by a moderate slope depending on the shape of the liquidus temperature. In this approach the eutectic melt fraction jump is approximated by a melting curve with a steep but finite slope. This numerically strong temperature dependence requires strong damping with delay close to 1.

Appendix C: Derivation of the Analytical Scaling Law for Batholith Emplacement Versus Convective Recycling

We now derive an analytical scaling law for a boundary in the parameter space in Section 3.5 by defining a batholith emplacement parameter e_b . Emplacement of enriched silicic material takes place predominantly within the upper horizontal limb of the convective flow by segregation, that is, vertical porous flow of melt with a characteristic segregation velocity v_{sgr} out of solid material with horizontal viscous flow with a characteristic velocity u . This horizontal flow region represents the upper partially molten layer of convection, whose thickness can be denoted by $(a \cdot h)$, where h is the total thickness of the convecting layer, and a is the non-dimensional thickness of this upper layer. For sufficiently high Rayleigh number u scales with the Rayleigh number for bottom heat flux (Schubert et al., 2001)

$$u = \frac{\kappa}{h} b \text{Ra}_q^\gamma \quad (\text{C1})$$

where κ is the thermal diffusivity, b is a non-dimensional number ($= 0.632$ for constant viscosity convection with constant bottom heat flux), and γ is a power exponent ($= 1/2$). In this study, convection is driven by both thermal and melt buoyancy but is hampered by lighter enrichment material formed due to solidification. We modify the above scaling law by using an effective Rayleigh number

$$\text{Ra}_{\text{eff}} = \text{Ra}_q + \varphi \text{Ra}_f - e \text{Ra}_{\text{enr}} \quad (\text{C2})$$

where the Rayleigh numbers are defined in Equation 4, φ is an average melt fraction in the partially molten region, and e gives the typical degree of enrichment within the upper part of the convection cell. The segregation velocity can be obtained from Darcy's law as

$$v_{\text{sgr}} = \frac{d^2 \varphi^{n_\varphi - 1} \Delta \rho_f g}{C \eta_f} \quad (\text{C3})$$

where η_f is the melt viscosity, C is a geometric constant of the order of 100 depending on the actual pore geometry, d is the mean distance between the pores (often equal to the grain size), n_φ is the power exponent of the permeability—porosity relation, $\Delta \rho_f = \rho_0 - \rho_{0f}$ is the difference between melt and reference density, and g is the gravitational acceleration. We define the degree of batholith emplacement by the ratio of the time t_{hor} needed for a partially molten material volume to travel the horizontal distance within the upper part of the convection cell which scales with h , and the time t_{sgr} needed for the melt to segregate vertically across the distance ($a \cdot h$):

$$e_b \equiv \begin{cases} \frac{t_{\text{hor}}}{t_{\text{sgr}}} = \frac{v_{\text{sgr}}}{u a} & \text{if } t_{\text{sgr}} \geq t_{\text{hor}} \\ 1 & \text{if } t_{\text{sgr}} < t_{\text{hor}} \end{cases} \quad (\text{C4})$$

If $t_{\text{sgr}} \geq t_{\text{hor}}$ only a fraction of the available melt contributes to emplacement, and this fraction scales with the ratio of these times, that is, e_b . If $t_{\text{sgr}} < t_{\text{hor}}$ melt has enough time to fully segregate out of the partially molten horizontally flowing layer to form a batholith emplacement layer, and we truncate e_b at 1 to define the case of full emplacement. The non-dimensional layer thickness a will depend on how much melt solidifies at its top, that is, it depends on the buoyancy of the enriched solidified material. We describe this behavior by

$$a = a_0 \left(1 - \frac{e \text{Ra}_{\text{enr}}}{\text{Ra}_{\text{eff}}} \right) \quad (\text{C5})$$

with a_0 as thickness of this layer in the absence of solidification. The idea behind the definition Equation C5 is: Thinning of this layer due to batholith emplacement near its top scales with the contrast of buoyant density of the enriched solid material $\Delta \rho_{\text{enr}}$ times the typical enrichment e relative to the total buoyant density driving convection. This ratio can be written in terms of Rayleigh numbers, that is, $\frac{e \text{Ra}_{\text{enr}}}{\text{Ra}_{\text{eff}}}$, and the effective layer a can be defined by Equation C5. We now use Equation C1, replace the Rayleigh number by the effective Rayleigh number of Equation C2, and insert the two velocities and a from Equation C5 into Equation C4 to obtain, after some rearranging

$$e_b = \frac{\text{Ra}_f}{\text{Rt}} \frac{\varphi^{n_\varphi - 1}}{b a_0 \left(1 - \frac{e \text{Ra}_{\text{enr}}}{\text{Ra}_{\text{eff}}} \right) \text{Ra}_{\text{eff}}^\gamma} \quad (\text{C6})$$

truncated at 1.

The regime boundaries found in Figures 17a–17c can be described by defining the boundary as those parameter combinations Rt , and Ra_{enr} at which the emplacement parameter e_b is equal to $e_{b05} = 0.5$. Inserting this value into Equation C6 gives the boundary retention number $\text{Rt}_b = \text{Rt}(\text{Ra}_{\text{enr}}, e_b = e_{b05})$. We can rewrite this equation in dimensional form by solving for the least known parameters melt viscosity as a function of mean distances between pores or channels

$$\eta_f |_{\text{boun}} = \frac{\Delta \rho_f g h d^2 \varphi^{n_\varphi - 1}}{\kappa C e_{b05} b a_0 \left(1 - \frac{\Delta \rho_{\text{enr}} e}{\frac{\rho_0 a g h}{\lambda} + \Delta \rho_f \varphi - \Delta \rho_{\text{enr}} e} \right) \text{Ra}_{\text{eff}}^\gamma} \quad (\text{C7})$$

Appendix D: More Details on the Effect of Density of the Enriched Felsic Rock and the Physics of Convective Recycling and Batholith Emplacement

In Section 3.2 models have been shown in which the density of the enriched felsic rock has been systematically varied. Here some more details are discussed. Figures D1a and D1c show that the models with batholith emplacement (red and pink curves) are characterized by acceleration of enrichment and melt fraction after about 4–6 Ma, while the convective recycling models show a nearly steady increase. Batholith emplacement is accompanied by RMS segregation velocities and solid velocities that are of the same order of magnitude at around 10 Ma (Figures D1b and D1d). In contrast, the recycling models show significantly larger RMS solid velocities than segregation velocities. The solid velocities of the batholith emplacement models first increase with time as the models heat up. After 4 (pink curve) or 6 Ma (red curve) the RMS solid velocities decrease with time because the active part of the convecting crust progressively becomes thinner beneath the accumulated enriched layer, which does not participate in the flow anymore. The green and blue curves (Figure D1d), however, increase over the full 10 Ma duration of the heat pulse, because the convecting layer progressively thickens as hot material reaches increasingly shallower regions, but is continuously recycled.

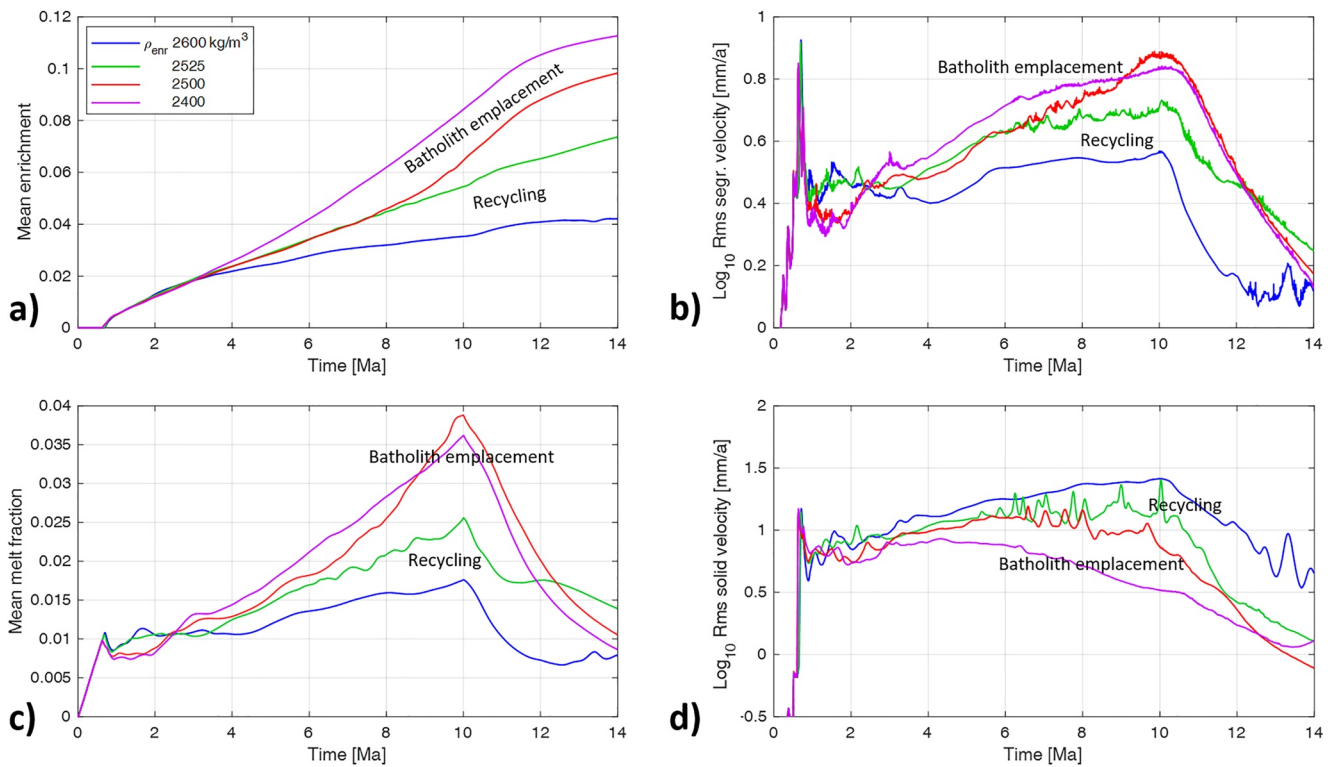


Figure D1. Effect of different densities of enriched material. Temporal evolution of (a) mean enrichment, (b) root mean square (RMS) segregation velocity, (c) mean melt fraction, and (d) RMS solid velocity of four selected models covering the bifurcation density of 2,525 kg/m³ between recycling and batholith emplacement of the single pulse models.

A similar behavior is observed for the pulsed models (Figure D2): Starting from the first pulse, the lowest density model (2,500 kg/m³, pink curve) departs from the others as enriched silicic material underplates the upper crust and is not dragged back into the lower crust. Already during the first pulse, the segregation and solid velocities of the pink model are of similar order, and during the later pulses, segregation velocities exceed the solid velocities reinforcing strong batholith emplacement. The 2,550 kg/m³ model (red curve) is transitional between batholith emplacement and recycling: until the end of the second pulse, it follows the same trend as the two denser models (blue and green lines in Figure D2), with recycling. At that time (around 8 Ma) the 2,550 kg/m³ model deviates from the other two and batholiths of enriched material form as in the case of 2,500 kg/m³ density model.

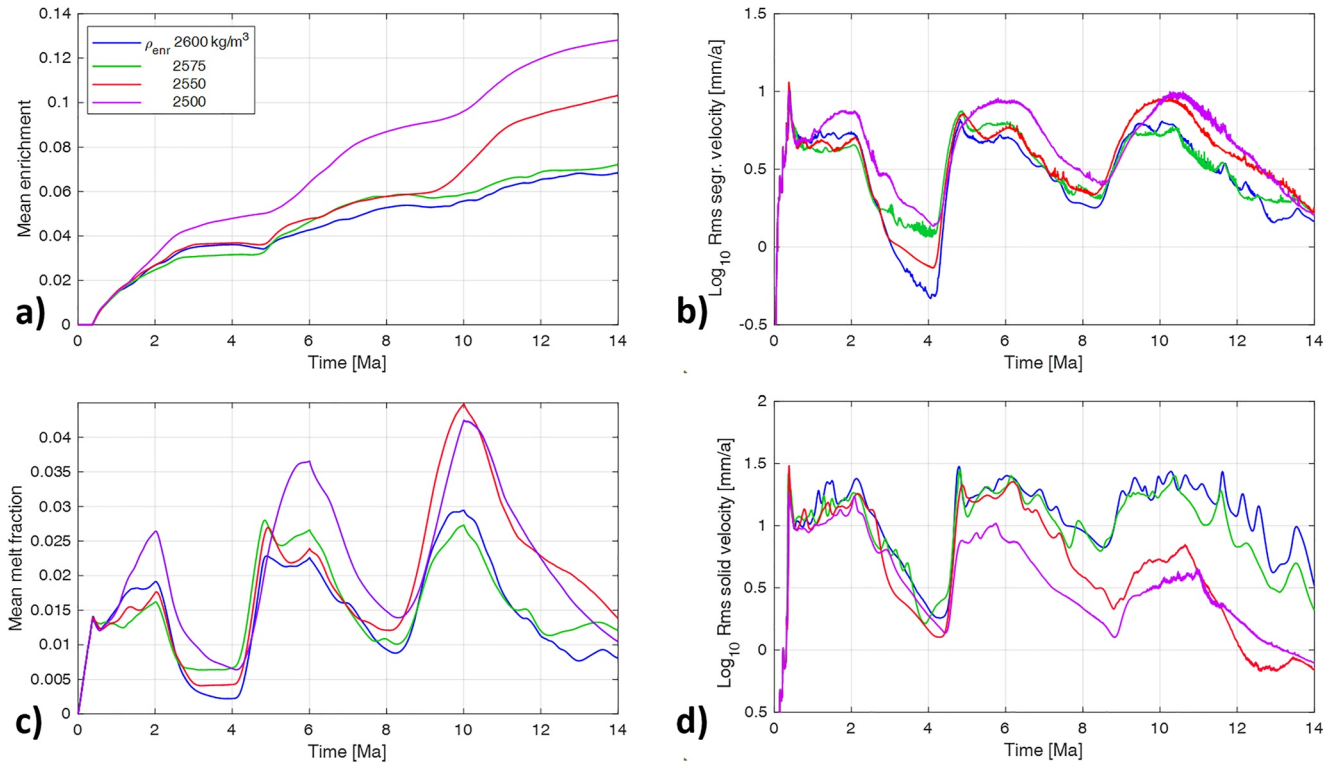


Figure D2. Effect of different densities of enriched rocks. Temporal evolution of (a) mean enrichment, (b) root mean square (RMS) segregation velocity, (c) mean melt fraction, and (d) RMS solid velocity of four selected models covering the bifurcation density of 2,555 kg/m³ between recycling and batholith emplacement of the multiple pulse models.

The models in Figure 15a with $\rho_{\text{enr}} = 2,600 \text{ kg/m}^3$ (model sing1d in Figure D3) and with $\rho_{\text{enr}} = 2,500 \text{ kg/m}^3$ (model sing3a) can be used to elucidate the physics responsible for convective recycling and batholith emplacement, respectively. Figure D3 shows these models at 10 Ma. In the recycling case of model sing1d (Figures D3a, D3c, and D3e), the convection cycle undergoes melting in the lower crust and in the rising limb of the flow, while freezing occurs mostly in the upper horizontal part and early in the downwelling limb. This is typical of phase-change-driven convection: most of the enriched material forming at the freezing front is incorporated into the downwelling flow and this solidified material remelts preferentially because of its lower solidus temperature as it reaches the base of the convection cell. In the batholith emplacement model sing3a (Figures D3b, D3d, and D3f), freezing dominates in the upper part of the rising limb, and the frozen material is displaced horizontally with only some material being recycled into the downwelling flow (blue middle part in Figures D3b and D3d). The reason for freezing in the top part of the rising flow is the enhanced segregation: The fluid has a considerably faster upwelling velocity compared to the solid (about two times). This can be seen in the divergence of the black and gray arrows in Figure D3d and contributes to the differentiation and emplacement of enriched, buoyant material in the uppermost region of the diapir/plume. Compared to the strong segregation in Figure D3b, the segregation velocity in Figure D3a is slower, only about 20% of the solid velocity. In this case, melt does not have enough time to leave its host rock and to freeze before it is recycled. Note that the local ratio of segregation to solid velocity may be much larger than the RMS averaged ratio: locally the ratio can reach a factor 3 (e.g., Figure D3d, depth range 25–30 km), while RMS averaged ratio is just about unit at 10 Ma. Only during the late stage (10–14 Ma) of this model the RMS segregation velocity continuously exceeds the solid velocity and builds up a well-developed enriched body (see Figure 15a, model with 2,500 kg/m³). In contrast, even at late stages, the RMS segregation velocity of the recycling model (Figure D3e) stays well below the solid velocity and no enriched body forms (see Figure 15a, left model with 2,600 kg/m³).

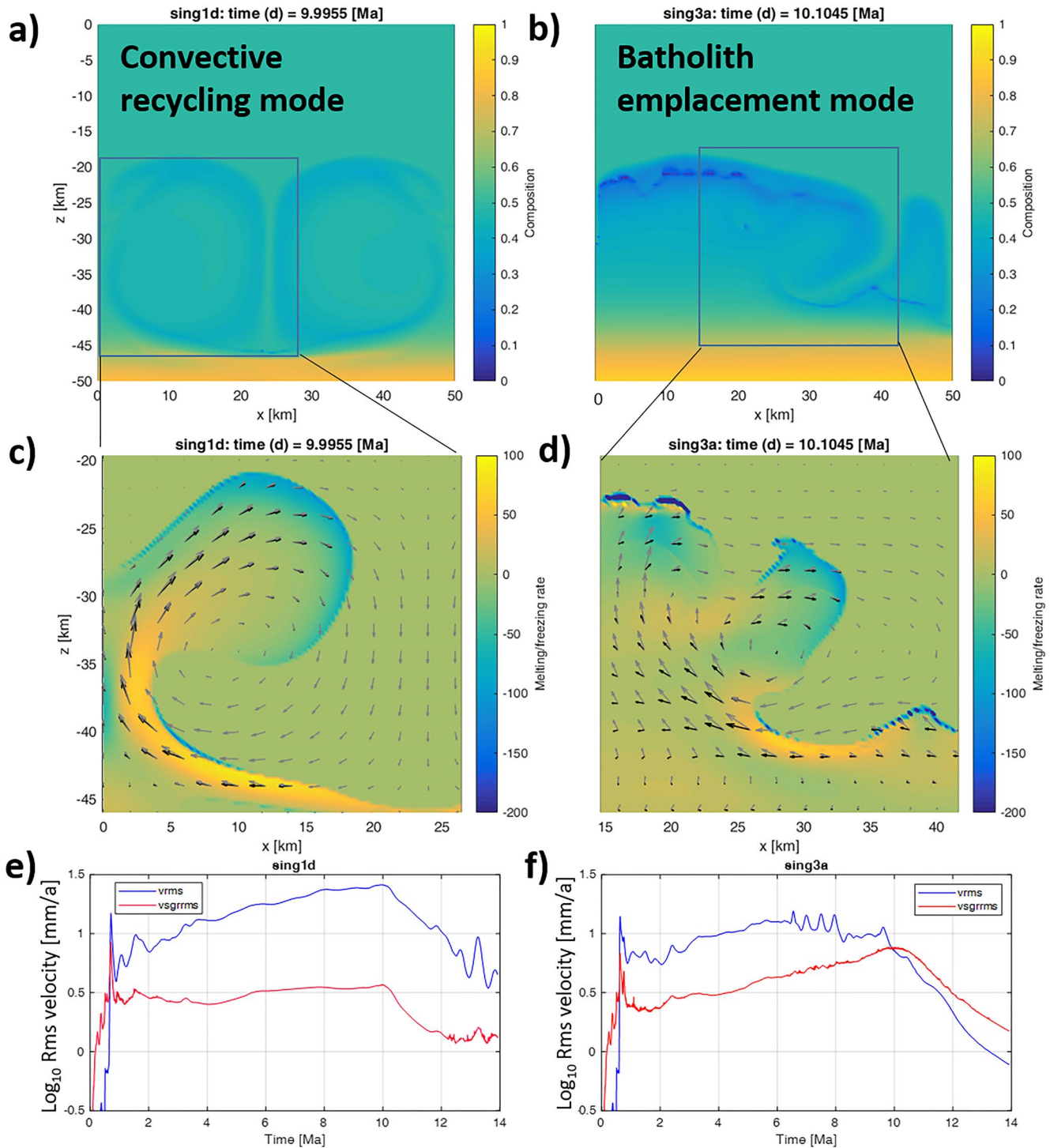


Figure D3. Comparison of models representing the convective recycling mode (left, panels (a, c, and e) and the batholith emplacement mode (right, panels (b, d, and f). All parameters are the same except the enrichment densities, which correspond to $Ra_{enr} = 1,350$ or $\rho_{enr} = 2,600 \text{ kg/m}^3$ (left model) and $Ra_{enr} = 2,700$ or $\rho_{enr} = 2,500 \text{ kg/m}^3$ (right model). For both models, a single heat pulse of 10 Ma duration was assumed, $Ra_q = 1450$ (corresponding to 84 mW/m^2 , and $Rt = 3$ (similar to Figure 3). The resulting mean enrichment at the end of the model run (14 Ma) is 0.04 (left model) and 0.098 (more than double on right model). In panels (a, b) the colors show the composition at 10 Ma. In panels (c, d) the colors show the non-dimensional volumetric melting- or solidification rates, positive values in orange-red are melting rates and negative values in blue tones are solidification rates. To dimensionalize these rates they must be multiplied by $0.01168/\text{Ma}$ or $1.1168\%/\text{Ma}$. The black arrows show the solid velocity with a maximum vector length of (c) 81 and (d) 23 mm/a, the gray arrows show the fluid velocity with a maximum vector length of (c) 99 and (d) 41 mm/a. In panels (e, f) the logarithmic root mean square segregation (red, “vsgrms”) and solid (blue, “vrms”) velocities are shown as a function of time.

Inspecting the full-time evolution of the batholith emplacement model sing3a reveals that recycling of solidified enriched material continues until 5.5 Ma, as long as the RMS segregation to solid velocity ratio is well below $\sim 1/3$ (see Figure D3f, where the difference of the \log_{10} velocities is -0.5). Between 7.2 and 10 Ma the segregation velocity approaches the solid velocity and small melt rich bodies rise to the growing emplacement zone where they solidify without being incorporated into the downwelling flow. The mean enrichment of the model accelerates at this time (Figure D1a, red curve with $2,500 \text{ kg/m}^3$). At 10 Ma the two velocities become equal and the differentiation of enriched material strongly intensifies once more, which is indicated by the sharp drop of the solid velocity because no more thermal and melt buoyancy contributes to the convective circulation, while segregation dominates and continues to increase the size of the enriched batholith. This is also seen in the mean enrichment curve (Figure D1a, red curve) which has its strongest increasing rate between 10 and 12 Ma.

Data Availability Statement

The data of this paper consists of modeling results generated by the own developed code FDCON version 22.1a. The Fortran source code, the input and output data of the reference model (Figures 3b, 4, and 5d–5f), a few visualizing MATLAB routines and an instruction file “readme” are available on Zenodo under Schmeling (2023), <https://doi.org/10.5281/zenodo.7839871>.

Acknowledgments

This work was initiated during a sabbatical leave of H.S. and G.M. at Monash University, Melbourne. We thank for the warm hospitality, and especially Sandy Cruden for exciting and helpful discussions. This work has been supported by a Grant (SCHM 872/25-1) of the Deutsche Forschungsgemeinschaft. Open Access funding enabled and organized by Projekt DEAL.

References

- Annen, C., Blundy, D., & Sparks, R. S. J. (2006). The genesis of intermediate and silicic magmas in deep crustal hot zones. *Journal of Petrology*, *47*(3), 505–539. <https://doi.org/10.1093/ptrology/egi084>
- Annen, C., Blundy, J. D., Leuthold, J., & Parks, R. S. (2015). Construction and evolution of igneous bodies: Towards an integrated perspective of crustal magmatism. *Lithos*, *230*, 206–221. <https://doi.org/10.1016/j.lithos.2015.05.008>
- Arnold, J., Jacoby, W. R., Schmeling, H., & Schott, B. (2001). Continental collision and the dynamic and thermal evolution of the Variscan orogenic crustal root - Numerical models. *Journal of Geodynamics*, *31*(3), 273–291. [https://doi.org/10.1016/s0264-3707\(00\)00023-5](https://doi.org/10.1016/s0264-3707(00)00023-5)
- Babeyko, A. Y., Sobolev, S. V., Trumbull, R. B., Oncken, O., & Lavier, L. (2002). Numerical models of crustal scale convection and partial melting beneath the Altiplano-Puna plateau. *Earth and Planetary Science Letters*, *199*(3–4), 373–388. [https://doi.org/10.1016/s0012-821x\(02\)00597-6](https://doi.org/10.1016/s0012-821x(02)00597-6)
- Bachmann, O., & Huber, C. (2016). Silicic magma reservoirs in the Earth's crust. *American Mineralogist*, *101*(11), 2377–2404. <https://doi.org/10.2138/am-2016-5675>
- Bittner, D., & Schmeling, H. (1995). Numerical modelling of melting processes and induced diapirism in the lower crust. *Geophysical Journal International*, *123*(1), 59–70. <https://doi.org/10.1111/j.1365-246X.1995.tb06661.x>
- Blundy, J. D., & Annen, C. J. (2016). Crustal magmatic systems from the perspective of heat transfer. *Elements*, *12*(2), 115–120. <https://doi.org/10.2113/gselements.12.2.115>
- Cashman, K. V., Sparks, R. S. J., & Blundy, J. D. (2017). Vertically extensive and unstable magmatic systems: A unified view of igneous processes. *Science*, *355*(6331), eaag3055. <https://doi.org/10.1126/science.aag3055>
- Chappell, B. W., & White, A. J. R. (2001). Two contrasting granite types: 25 years later. *Australian Journal of Earth Sciences*, *48*(4), 489–499. <https://doi.org/10.1046/j.1440-0952.2001.00882.x>
- Chappell, B. W., White, A. J. R., & Wyborn, D. (1987). The importance of residual source material (restite) in granite petrogenesis. *Journal of Petrology*, *28*(6), 1111–1138. <https://doi.org/10.1093/ptrology/28.6.1111>
- Clemens, J. D., & Vielzeuf, D. (1987). Constraints on melting and magma production in the crust. *Earth and Planetary Science Letters*, *86*(2–4), 287–306. [https://doi.org/10.1016/0012-821x\(87\)90227-5](https://doi.org/10.1016/0012-821x(87)90227-5)
- Clemens, J. D. (2005). Melting of the continental crust I: Fluid regimes, melting reactions and source-rock fertility. In M. Brown & T. Rushmer (Eds.), *Evolution and differentiations of the continental crust* (pp. 297–331). Cambridge University Press.
- Comeau, M. J., Unsworth, M. J., Ticona, F., & Sunagua, M. (2015). Magnetotelluric images of magma distribution beneath Volcan Uturuncu, Bolivia: Implications for magma dynamics. *Geology*, *43*(3), 243–246. <https://doi.org/10.1130/g36258.1>
- Cruden, A. R., Koyi, H., & Schmeling, H. (1995). Diapiric basal entrainment of mafic into felsic magma. *Earth and Planetary Science Letters*, *131*(3–4), 321–340. [https://doi.org/10.1016/0012-821x\(95\)00033-9](https://doi.org/10.1016/0012-821x(95)00033-9)
- de Silva, S. L., & Gosnold, W. D. (2007). Episodic construction of batholiths: Insights from the spatiotemporal development of an ignimbrite flare-up. *Journal of Volcanology and Geothermal Research*, *167*(1–4), 320–335. <https://doi.org/10.1016/j.jvolgeores.2007.07.015>
- de Silva, S. L., Riggs, N. R., & Barth, A. P. (2015). Quickening the pulse: Fractal tempos in continental arc magmatism. *Elements*, *11*(2), 113–118. <https://doi.org/10.2113/gselements.11.2.113>
- del Potro, R., Diez, M., Blundy, J., Camacho, A. G., & Gottsmann, J. (2013). Diapiric ascent of silicic magma beneath the Bolivian Altiplano. *Geophysical Research Letters*, *40*(10), 2044–2048. <https://doi.org/10.1002/grl.50493>
- Fialko, Y., & Pearce, J. (2012). Sombrero uplift above the Altiplano-Puna magma body: Evidence of a ballooning mid-crustal diapir. *Science*, *338*(6104), 250–252. <https://doi.org/10.1126/science.1226358>
- Folkes, C. B., de Silva, S. L., Schmitt, A. K., & Cas, R. A. F. (2011). A reconnaissance of U-Pb zircon ages in the Cerro Galán system, NW Argentina: Prolonged magma residence, crystal recycling, and crustal assimilation. *Journal of Volcanology and Geothermal Research*, *206*(3–4), 136–147. <https://doi.org/10.1016/j.jvolgeores.2011.06.001>
- Frost, B. R., Barnes, C. G., Collins, W. J., Arculus, R. J., Ellis, D. J., & Frost, C. D. (2001). A geochemical classification for granitic rocks. *Journal of Petrology*, *42*(11), 2033–2048. <https://doi.org/10.1093/ptrology/42.11.2033>
- Gottsmann, J., Blundy, J., Henderson, S., Pritchard, M. E., & Sparks, R. S. J. (2017). Thermomechanical modeling of the Altiplano-Puna deformation anomaly: Multiparameter insights into magma mush reorganization. *Geosphere*, *13*(4), 1042–1065. <https://doi.org/10.1130/GES01420.1>
- Guo, Z., & Wilson, M. (2019). Late Oligocene–early Miocene transformation of postcollisional magmatism in Tibet. *Geology*, *47*(8), 776–780. <https://doi.org/10.1130/G46147.1>

- Hasalová, P., Weinberg, R., Ward, L., & Fanning, C. M. (2013). Diatexite deformation and magma extraction on Kangaroo Island, South Australia. In *EGU General Assembly Conference Abstracts* (p. EGU20136524).
- Hering, P., González-Castillo, L., Castro, C., Junge, A., Brown, C., Márquez-Ramírez, V. H., et al. (2022). Tectonic controls on magmatic systems: Evidence from a three-dimensional anisotropic electrical resistivity model of Ceboruco Volcano. *Journal of Volcanology and Geothermal Research*, 428, 107382. <https://doi.org/10.1016/j.jvolgeores.2021.107382>
- Horton, F., & Leech, M. L. (2013). Age and origin of granites in the Karakoram shear zone and Greater Himalaya Sequence, NW India. *Lithosphere*, 5(3), 300–320. <https://doi.org/10.1130/L213.1>
- Jagoutz, O., & Klein, B. (2018). On the importance of crystallization – Differentiation for the generation of SO_2 -rich melts and the compositional build-up of arc (and continental) crust. *American Journal of Science*, 318(1), 29–63. <https://doi.org/10.2475/01.2018.03>
- Katz, R. F., Knepley, M. G., Smith, N., Spiegelman, M., & Coon, E. T. (2007). Numerical simulation of geodynamic processes with the portable extensible toolkit for scientific computation. *Physics of the Earth and Planetary Interiors*, 163(1–4), 52–68. <https://doi.org/10.1016/j.pepi.2007.04.016>
- Keller, T., & Suckale, J. (2019). A continuum model of multi-phase reactive transport in igneous systems. *Geophysical Journal International*, 219(1), 185–222. <https://doi.org/10.1093/gji/ggz287>
- Kern, J. M., de Silva, S. L., Schmitt, A. K., Kaiser, J. F., Iriarte, A. R., & Economos, R. (2016). Geochronological imaging of an episodically constructed subvolcanic batholith: U-Pb in zircon chronochemistry of the Altiplano-Puna volcanic complex of the central Andes. *Geosphere*, 12(4), 1054–1077. <https://doi.org/10.1130/GES01258.1>
- Kirby, S. H., & Kronenberg, A. K. (1987). Rheology of the lithosphere: Selected topics. *Reviews of Geophysics*, 25(6), 1219–1244. <https://doi.org/10.1029/RG025i006p01219>
- Lederer, G. W., Cottle, J. M., Jessup, M. J., Langille, J. M., & Ahmad, T. (2013). Time-scales of partial melting in the Himalayan middle crust: Insight from the Leo Pargil dome, northwest India. *Contributions to Mineralogy and Petrology*, 166(5), 1415–1441. <https://doi.org/10.1007/s00410-013-0935-9>
- Leuthold, J., Müntener, O., Baumgartner, L. P., Putlitz, B., Ovtcharov, M., & Schaltegger, U. (2012). Time resolved construction of a bimodal laccolith (Torres del Paine, Patagonia). *Earth and Planetary Science Letters*, 325–326, 85–92. <https://doi.org/10.1016/j.epsl.2012.01.032>
- Li, J., Ding, X., & Liu, J. (2022). The role of fluids in melting the continental crust and generating granitoids: An overview. *Geosciences*, 12(8), 285. <https://doi.org/10.3390/geosciences12080285>
- Louis-Napoléon, A., Bonometti, T., Gerbault, M., Martin, R., & Vanderhaeghe, O. (2022). Models of convection and segregation in heterogeneous partially molten crustal roots with a VOF method – I: Flow regimes. *Geophysical Journal International*, 229(3), 2047–2080. <https://doi.org/10.1093/gji/ggab510>
- Ma, K.-F., Wang, J.-H., & Zhao, D. (1996). Three dimensional seismic velocity structure of the crust and uppermost mantle beneath Taiwan. *Journal of Physics of the Earth*, 44(2), 85–105. <https://doi.org/10.4294/jpe1952.44.85>
- McKenzie, D. (1984). The generation and compaction of partially molten rock. *Journal of Petrology*, 25(3), 713–765. <https://doi.org/10.1093/ptrology/25.3.713>
- Moyen, J.-F., Janoušek, V., Laurent, O., Bachmann, O., Jacob, J.-B., Farina, P., et al. (2021). Crustal melting vs. fractionation of basaltic magmas: Part 1, the bipolar disorder of granite petrogenetic models. *Lithos*, 402, 106291. <https://doi.org/10.1016/j.lithos.2021.106291>
- Nelson, K. D., Zhao, W., Brown, L. D., Kuo, J., Che, J., Liu, X., et al. (1996). Partially molten middle crust beneath southern Tibet: Synthesis of project INDEPTH results. *Science*, 274(5293), 1684–1688. <https://doi.org/10.1126/science.274.5293.1684>
- Othman, D. B., Polvé, M., & Allègre, C. J. (1984). Nd—Sr isotopic composition of granulites and constraints on the evolution of the lower continental crust. *Nature*, 307(5951), 510–515. <https://doi.org/10.1038/307510a0>
- Perkins, J. P., Ward, K. M., de Silva, S. L., Zandt, G., Beck, S. L., & Finnegan, N. J. (2016). Surface uplift in the central Andes driven by growth of the Altiplano Puna magma body. *Nature Communications*, 7(1), 13185. <https://doi.org/10.1038/ncomms13185>
- Puxeddu, M. (1984). Structure and late Cenozoic evolution of the upper lithosphere in Southwest Tuscany (Italy). *Tectonophysics*, 101(3–4), 357–382. [https://doi.org/10.1016/0040-1951\(84\)90121-5](https://doi.org/10.1016/0040-1951(84)90121-5)
- Read, H. H. (1948). Granites and granites. In J. Gilluly (Ed.), *Origin of granite* (Vol. 28, pp. 1–19). Geological Society of America Memoirs.
- Ribe, N. M. (1985). The generation and composition of partial melts in the Earth's mantle. *Earth and Planetary Science Letters*, 73(2–4), 361–376. [https://doi.org/10.1016/0012-821x\(85\)90084-6](https://doi.org/10.1016/0012-821x(85)90084-6)
- Riel, N., Mercier, J., & Weinberg, R. (2016). Convection in a partially molten metasedimentary crust? Insights from the El Oro complex (Ecuador). *Geology*, 44(1), 31–34. <https://doi.org/10.1130/G37208.1>
- Rivalta, E., Taisne, B., Buger, A. P., & Katz, R. F. (2015). A review of mechanical models of dike propagation: Schools of thought, results and future directions. *Tectonophysics*, 638, 1–42. <https://doi.org/10.1016/j.tecto.2014.10.003>
- Rubatto, D., Chakraborty, S., & Dasgupta, S. (2013). Timescales of crustal melting in the Higher Himalayan Crystallines (Sikkim, Eastern Himalaya) inferred from trace element-constrained monazite and zircon chronology. *Contributions to Mineralogy and Petrology*, 165(2), 349–372. <https://doi.org/10.1007/s00410-012-0812-y>
- Rubin, A. M. (1993). Tensile fracture of rock at high confining pressure Implication for dike propagation. *Journal of Geophysical Research*, 98(B9), 15919–15935. <https://doi.org/10.1029/93jb01391>
- Rummel, L., Kaus, B. J. P., Baumann, T. S., White, R. W., & Riel, N. (2020). Insights into the compositional evolution of crustal magmatic systems from coupled petrological-geodynamical models. *Journal of Petrology*, 61(2), ega029. <https://doi.org/10.1093/ptrology/egaa029>
- Schmelting, H. (2023). FDCON source code and input files corresponding to dynamic two-phase flow modelling of melt segregation in continental crust: Batholith emplacement vs. crustal convection, with implications for magmatism in thickened plateaus [Software, Dataset]. Zenodo. <https://doi.org/10.5281/zenodo.7839871>
- Schmelting, H., Kruse, J.-P., & Richard, G. (2012). Effective shear and bulk viscosity of partially molten rock based on elastic moduli theory of a fluid filled poroelastic medium. *Geophysical Journal International*, 190(3), 1571–1578. <https://doi.org/10.1111/j.1365-246X.2012.05596.x>
- Schmelting, H., Marquart, G., Weinberg, R., & Wallner, H. (2019). Modelling melting and melt segregation by two-phase flow: New insights into the dynamics of magmatic systems in the continental crust. *Geophysical Journal International*, 217(1), 422–450. <https://doi.org/10.1093/gji/ggz029>
- Schön, J. H. (2015). *Physical properties of rocks: Fundamentals and principles of petrophysics* (p. 512). Elsevier.
- Schubert, G., Turcotte, D. L., & Olson, P. (2001). *Mantle convection in the Earth and planets*. Cambridge University Press.
- Seporian, G., Rust, A. C., & Sparks, R. S. J. (2018). The gravitational stability of lenses in magma mushes: Confined Rayleigh-Taylor instabilities. *Journal of Geophysical Research: Solid Earth*, 123(5), 3593–3607. <https://doi.org/10.1029/2018JB015523>
- Spang, A., Baumann, T. S., & Kaus, B. J. P. (2021). A multiphysics approach to constrain the dynamics of the Altiplano-Puna magmatic system. *Journal of Geophysical Research: Solid Earth*, 126(7), e2021JB021725. <https://doi.org/10.1029/2021JB021725>

- Sparks, R. S. J., Annen, C., Blundy, J. D., Cashman, K. V., Rust, A. C., & Jackson, M. D. (2019). Formation and dynamics of magma reservoirs. *Philosophical Transactions of the Royal Society A*, *377*(2139), 20180019. <https://doi.org/10.1098/rsta.2018.0019>
- Springer, M. (1999). Interpretation of heat-flow density in the central Andes. *Tectonophysics*, *306*(3–4), 377–395. [https://doi.org/10.1016/S0040-1951\(99\)00067-0](https://doi.org/10.1016/S0040-1951(99)00067-0)
- Springer, M., & Förster, A. (1998). Heat-flow density across the Central Andean subduction zone. *Tectonophysics*, *291*(1–4), 123–139. [https://doi.org/10.1016/S0040-1951\(98\)00035-3](https://doi.org/10.1016/S0040-1951(98)00035-3)
- Symington, N. J., Weinberg, R. F., Hasalová, P., Wolfram, L. C., Raveggi, M., & Armstrong, R. A. (2014). Multiple intrusions and remelting-remobilization events in a magmatic arc: The St. Peter Suite, South Australia. *Geological Society of America Bulletin*, *126*(9–10), 1200–1218. <https://doi.org/10.1130/B30975.1>
- Thybo, H., & Artemieva, I. M. (2013). Moho and magmatic underplating in continental lithosphere. *Tectonophysics*, *609*, 605–619. <https://doi.org/10.1016/j.tecto.2013.05.032>
- Unsworth, M., Jones, A., Wei, W., Marquis, G., Gokarn, S. G., & Spratt, J. E. (2005). Crustal rheology of the Himalaya and Southern Tibet inferred from magnetotelluric data. *Nature*, *438*(7064), 78–81. <https://doi.org/10.1038/nature04154>
- Vanderhaeghe, O., Kruckenberg, S. C., Gerbault, M., Martin, L., Duchêne, S., & Deloule, E. (2018). Crustal-scale convection and diapiric upwelling of a partially molten orogenic root (Naxos dome, Greece). *Tectonophysics*, *746*, 459–469. <https://doi.org/10.1016/j.tecto.2018.03.007>
- Van Zalinge, M. E., Mark, D. F., Sparks, R. S. J., Tremblay, M. M., Keller, C. B., Cooper, F. J., & Rust, A. (2022). Timescales for pluton growth, magma-chamber formation and super-eruptions. *Nature*, *608*(7921), 87–92. <https://doi.org/10.1038/s41586-022-04921-9>
- Viskupic, K., Hodges, K. V., & Bowring, S. A. (2005). Timescales of melt generation and the thermal evolution of the Himalayan metamorphic core, Everest region, eastern Nepal. *Contributions to Mineralogy and Petrology*, *149*, 1–21. <https://doi.org/10.1007/s00410-004-0628-5>
- Wang, Q., Hawkesworth, C., Wyman, D., Chung, S. L., Wu, F. Y., Li, X. H., et al. (2016). Pliocene-Quaternary crustal melting in central and northern Tibet and insights into crustal flow. *Nature Communications*, *7*(1), 11888. <https://doi.org/10.1038/ncomms11888>
- Ward, K. M., Zandt, G., Beck, S. L., Christensen, D. H., & McFarlin, H. (2014). Seismic imaging of the magmatic underpinnings beneath the Altiplano-Puna volcanic complex from the joint inversion of surface wave dispersion and receiver functions. *Earth and Planetary Science Letters*, *404*, 43–53. <https://doi.org/10.1016/j.epsl.2014.07.022>
- Weinberg, R. F. (2016). Himalayan leucogranites and migmatites: Nature, timing and duration of anatexis. *Journal of Metamorphic Geology*, *34*(8), 821–843. <https://doi.org/10.1111/jmg.12204>
- Weinberg, R. F. (1997). Diapir-driven crustal convection: Decompression melting, renewal of the magma source and the origin of nested plutons. *Tectonophysics*, *271*(3–4), 217–229. [https://doi.org/10.1016/S0040-1951\(96\)00269-7](https://doi.org/10.1016/S0040-1951(96)00269-7)
- Weinberg, R. F., & Hasalová, P. (2015). Water-flux melting of continental crust: A review. *Lithos*, *212–215*, 158–188. <https://doi.org/10.1016/j.lithos.2014.08.021>
- Weinberg, R. F., Vernon, R. H., & Schmeling, H. (2021). Processes in mushes and their role in the differentiation of granitic rocks. *Earth-Science Reviews*, *220*, 103665. <https://doi.org/10.1016/j.earscirev.2021.103665>
- Wells, P. R. A. (1980). Thermal models for the magmatic accretion and subsequent metamorphism of continental crust. *Earth and Planetary Science Letters*, *46*(2), 253–265. [https://doi.org/10.1016/0012-821x\(80\)90011-4](https://doi.org/10.1016/0012-821x(80)90011-4)
- Wells, P. R. A. (1981). Accretion of continental crust: Thermal and geochemical consequences. *Philosophical Transactions of the Royal Society of London, Series A*, *301*, 347–357.
- Wong, Y.-Q., & Keller, T. (2023). A unified numerical model for two-phase porous, mush and suspension flow dynamics in magmatic systems. *Geophysical Journal International*, *233*(2), ggac481. <https://doi.org/10.1093/gji/ggac481>
- Wyllie, P. J. (1984). Constraints imposed by experimental petrology on possible and impossible magma sources and products. *Philosophical Transactions of the Royal Society of London*, *A310*, 439–456.
- Zandt, G., Velasco, A. A., & Beck, S. L. (1994). Composition and thickness of the southern Altiplano crust, Bolivia. *Geology*, *22*(11), 1003–1006. [https://doi.org/10.1130/0091-7613\(1994\)022<1003:catots>2.3.co;2](https://doi.org/10.1130/0091-7613(1994)022<1003:catots>2.3.co;2)